nature communications

Article | Article in Press

https://doi.org/10.1038/s41467-026-78131-6

Viscoelasticity of synthetic antigen presenting cells reprograms T cell metabolism for TCR-T cell manufacturing and therapy

Received: 3 March 2026

Accepted: 16 September 2026

Published online: 20 November 2026

Check for updates

Youcheng Yang[1,15], Yan-Ruide Li[1,2,15], Zeyang Liu[1,15], Hao Zhou[3,4], Yichen Zhu[1,2], Xinyuan Shen[1,2], Dexter Lai[5], Yihui Cen[6], Emily Z. Y. Miller[7], Haochen Nan[1], Bo Zhang[1], Shubing Wang[1], Jason Lin[1], Yuning Chen[1,2], Bella Raykowski[3], Enbo Zhu[1,2,8], Jun Shen[9], Keyue Shen[3,10], Junyoung O. Park[1,5], Jingyi Jessica Li[6,11], Xiling Shen[7], Zhaohui Wang[7], Lili Yang[1,2,12,13,14] ✉ & Song Li[1,13,14] ✉

Adoptive T cell receptor (TCR)–based immunotherapy offers a powerful strategy to target solid tumors. However, how the physical properties of the antigen-presenting interface regulate T cell metabolic programming remains poorly defined. Here we develop synthetic viscoelastic activating cells (SynVAC), artificial antigen-presenting cells whose stress-relaxation kinetics are chemically tuned independently of stiffness and of peptide–MHC (pMHC) and co-stimulatory ligand density. SynVAC-pMHC provides a defined, scalable platform that outperforms monocyte-derived dendritic cells to enrich antigen-specific $CD8^+$ T cells. Fast-relaxing SynVAC-pMHC amplifies TCR signaling and mTOR activity, drives metabolic remodeling, and programs antigen-specific T cells toward an energetically favorable state with improved memory-like features after expansion. TCR-T cells expanded using fast-relaxing SynVAC-pMHC exhibit superior persistence and durable antitumor activity in melanoma and ovarian cancer models. These results establish cell-mimetic viscoelasticity as a key biophysical cue governing T cell metabolism and differentiation and offer a fully synthetic strategy for manufacturing potent TCR-T cells.

T cell receptor T cell therapy (TCR-T) offers a powerful strategy to target solid tumors by recognizing both cell surface antigens and intracellular tumor antigens presented by MHC[1–3]. This treatment begins by extracting T cells from a patient's blood and modifying their TCRs, or by expanding certain T cell populations that recognize and attack cancer cells expressing specific antigens, such as NY-ESO-1, MAGE-A3, and MART-1[4,5]. Nevertheless, existing TCR-T manufacturing platforms continue to encounter significant challenges. For example, monocyte-derived dendritic cells (moDCs) are commonly used for antigen-specific T cell activation; however, they exhibit limited fidelity to naturally circulating dendritic cell subsets and are typically generated under inflammatory conditions that may not recapitulate native antigen presentation. Consequently, moDC-based expansion is associated with suboptimal in vitro proliferation, accelerated phenotypic exhaustion, and limited in vivo persistence following infusion, as well

A full list of affiliations appears at the end of the paper. ✉e-mail: liliyang@ucla.edu; songli@ucla.edu

as donor-to-donor variability, poor scalability, and poorly controlled paracrine signaling[6,7].

Another widely used in vitro T cell activation method before TCR modification, stimulation with polystyrene beads coated with anti-CD3/CD28 antibodies or human leukocyte antigen–immunoglobulin fusion protein (HLA-Ig) and CD28-specific antibody, often triggers excessive stimulation, rapid T cell differentiation, and low T memory stem cells (TMSCs)[8–11]. To address these challenges, there is a critical need to develop next-generation aAPCs that not only deliver precise antigenic and costimulatory cues but also mimic the biophysical context of natural antigen presentation. Such platforms may enable the expansion of metabolically fit, memory-enriched T cells with improved persistence and tumor-clearing potential, thereby advancing the efficacy of TCR-T cell therapy against solid tumors.

Mechanical cues represent a fundamental but often underappreciated dimension of immune regulation, complementing the well-established roles of biochemical and cytokine-mediated signaling[12–15]. In T cells, mechanotransduction through TCR at the immune synapse regulates activation strength, cytokine secretion, and killing potency[16–21]. Notably, the stiffness of aAPCs within the physiological range of 1–30 kPa has been shown to optimize T cell activation and expansion[22–26]. In addition, the viscoelasticity of aAPCs or ECM, when using anti-CD3/CD28 as activation signals, enhances the stemness of expanded T cells[27,28]. However, the mechanisms by which viscoelastic cues influence T cell fate remain poorly understood. In parallel, accumulating evidence suggests that the metabolic fitness of T cells—including mitochondrial function, oxidative phosphorylation (OXPHOS) capacity, and balanced glycolytic activity—is a critical determinant of T cell differentiation and sustained antitumor immunity[29,30]. Whether and how the viscoelastic properties of antigen-presenting materials regulate T cell metabolic programming and differentiation remain open questions.

To better replicate the physiological cues of natural APCs, here we develop SynVAC-pMHC with tunable stress-relaxation kinetics that recapitulate their mechanical properties while presenting precisely defined pMHC and costimulatory ligands for antigen-specific TCR engagement. We find that fast-relaxing SynVAC-pMHC outperforms moDCs in promoting T cell expansion and memory enrichment of antigen-specific $CD8^+$ T cells via metabolic reprogramming. TCR-engineered T cells expanded on fast-relaxing SynVAC-pMHC exhibit durable in vivo persistence and superior antitumor efficacy across multiple solid tumor models. These findings establish viscoelasticity as a key biophysical regulator of TCR-driven T cell fate and position SynVAC-pMHC as a physiologically relevant, scalable platform for manufacturing potent TCR-T cell therapies.

Results

Fabrication of SynVAC-pMHC with tunable viscoelasticity

In previous studies, we have demonstrated that the viscoelastic properties of SynVAC coated with activating antibodies promote T-cell stemness and durability, and that a stiffness of 10 kPa is superior to 30 kPa[27]. Based on these findings, we designed a panel of SynVAC−pMHC constructs with varying stress-relaxation times while maintaining constant stiffness (8–10 kPa) and ligand density (Fig. 1a). These SynVAC-pMHC were used to investigate how mechanical relaxation influences antigen-specific T cell activation and function. In brief, four formulations of alginate-based microbeads (V1–V4) were engineered to exhibit half stress-relaxation times ranging from ~10 to ~700 s (Supplementary Fig. 1a). This mechanical property was measured using disc-shaped hydrogels (8 mm diameter, 2 mm thick) corresponding to each SynVAC-pMHC formulation, which were subjected to compressive mechanical testing. Atomic force microscopy (AFM) was further used to confirm their difference in viscoelasticity in the microbead formulation (Supplementary Fig. 1b). Furthermore, we confirmed that all formulations exhibited comparable stiffness, ensuring that differences among groups arose solely from variations in stress relaxation (Supplementary Fig. 1c). This design allowed us to isolate the effect of viscoelasticity on T cell activation dynamics.

Surface functionalization was performed using EDC/NHS chemistry to activate carboxyl groups on the alginate matrix, enabling conjugation of trans-cyclooctene (TCO) moieties. Subsequent click chemistry enabled attachment of tetrameric HLA-A*02:01/NY-ESO-1 (pMHC) and anti-CD28 antibodies to the bead surface, thereby facilitating antigen-specific T cell stimulation. This strategy was chosen for its high specificity and biocompatibility to covalently anchor tetrameric HLA-A*02:01/NY-ESO-1 complexes and anti-CD28 antibodies onto the bead surface.

To investigate the influence of viscoelasticity on antigen-specific T cell activation, SynVAC-pMHC (V1–V4) were cocultured with human peripheral blood mononuclear cells (PBMCs) pre-screened for HLA-A2 positivity. Flow cytometry at day 14 revealed that V1–V3 supported similar levels of NY-ESO-1-specific T (ESO-T) cell expansion, while V4 significantly underperformed in both metrics (Supplementary Fig. 1d, e). Furthermore, the in vitro tumor-killing assays showed that V4-expanded cells have significantly reduced tumor-killing ability against the tumor cell lines OVCAR3 and A375 (Supplementary Fig. 1f, g), suggesting an optimal range of SynVAC-pMHC viscoelasticity between 10 and 140 s. Based on the initial functional screen, V1 was selected as the fast-relaxing formulation because it represented the shortest stress-relaxation time and supported robust ESO-T expansion and tumor-killing activity. V4 was selected as an intermediate/medium-relaxing formulation because it represented the slowest-relaxing condition within the initial ionic alginate panel and showed reduced expansion and cytotoxic activity. To further extend the mechanical range, we also included a slow-relaxing formulation with an approximately 2000-s half-relaxation time, which served as a more elastic, slow-relaxation comparator. These three formulations were therefore designated fast-relaxing beads (FRB), medium-relaxing beads (MRB), and slow-relaxing beads (SRB), respectively.

Characterization of SynVAC-pMHC viscoelasticity and surface properties

To ensure that stiffness was not a confounding factor, AFM was used to measure the stiffness of FRB, MRB, and SRB, confirming uniformity across all groups (Fig. 1c). To further corroborate these findings, bulk gel analogs were also analyzed using a rheometer, which demonstrated FRBs displayed higher loss modulus (G″) (Fig. 1d) and tan δ (Fig. 1e) compared to MRBs and SRBs across tested frequencies, supporting their enhanced viscoelasticity.

To assess ligand density and distribution, flow cytometry was performed, showing consistent conjugation efficiency across all SynVAC-pMHC types (Fig. 1f). Confocal imaging further confirmed that ligand attachment was uniformly localized to the bead surface, thereby optimizing antigen presentation and cost-efficiency (Fig. 1g). Additionally, X-ray photoelectron spectroscopy (XPS) indicated similar calcium content in FRB and MRB beads, while SRB lacked calcium, reflecting its altered crosslinking profile (Fig. 1h).

Interaction of SynVAC-pMHC with ESO-T cells and activation potency

To visualize the initial physical interactions between antigen-specific T cells and SynVAC-pMHC, sorted ESO-T cells derived from human PBMCs were co-cultured with FRB for 1 h and analyzed by scanning electron microscopy (SEM). It revealed a close membrane contact and the formation of synapse-like structures between ESO-T cells and FRB, suggesting productive antigen recognition and engagement at the cell–bead interface (Supplementary Fig. 2). The morphological features of these contacts—such as membrane spreading, polarization, and tight junction formation—resemble the early stages of an immunological synapse, a hallmark of TCR-mediated recognition events.

https://doi.org/10.1038/s41467-026-78131-6

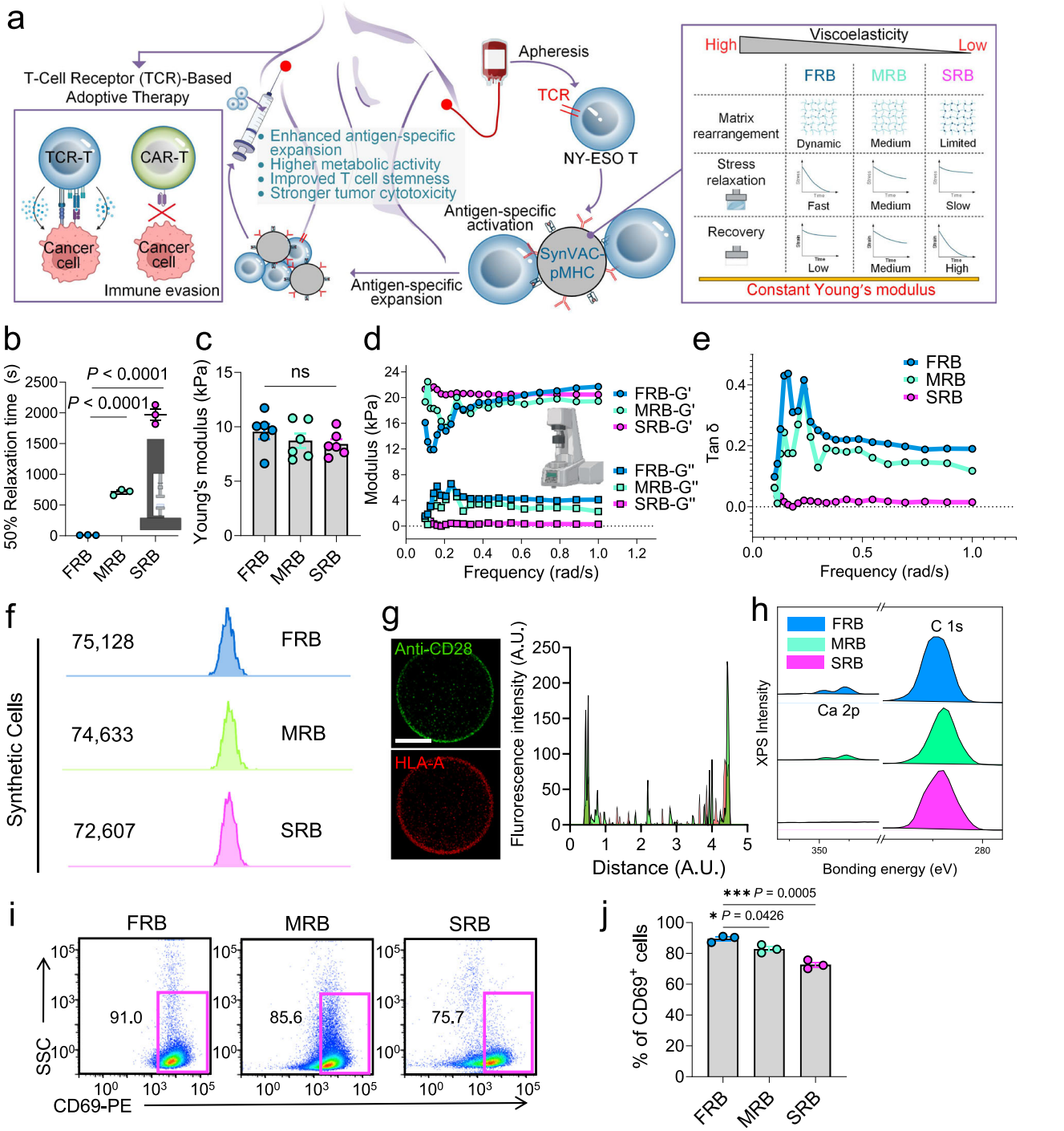


Fig. 1 | Mechanical characterization and ligand presentation of SynVAC-pMHC. **a** Schematic showing clinical procedures of TCR-T cell expansion for cancer therapy. The panel at the top right shows that SynVAC-pMHC can be fabricated with a constant Young's modulus but different viscoelastic properties, as characterized by stress relaxation time: FRB fast-relaxing bead, MRB medium-relaxing bead, and SRB slow-relaxing bead. The surface of SynVAC-pMHC is functionalized with peptide-MHC tetramer complex and anti-CD28, mimicking natural APCs to enhance TCR-T cell expansion with higher metabolic activity and stemness. Partially created in BioRender. Yang, Y. (2026) https://BioRender.com/pk28pj7. **b**, **c** Compressive testing confirms matched stiffness but distinct half stress-relaxation times across SynVAC-pMHC ($N = 3$). N represents the number of biologically independent samples. In (**b**), illustration is created in BioRender. Yang, Y. (2026) https://BioRender.com/pk28pj7. **d**, **e** Rheometry validates increased loss modulus (G″) and tan δ in FRBs, indicating enhanced viscoelasticity. Representative of 3 independent experiments. In (**d**), illustration is created in BioRender. Yang, Y. (2026) https://BioRender.com/pk28pj7. **f** Flow cytometry analysis of SynVAC-pMHC of different viscoelasticity confirms the equal ligand density. Representative of 3 independent experiments. **g** Confocal imaging of FRB showing the peptide-MHC and anti-CD28 are coated on the surface of the microbeads. Scale bar: 3 μm. Representative of 3 independent experiments. **h** X-ray photoelectron spectroscopy (XPS) revealed that FRB and MRB are ionically crosslinked with calcium ions, whereas SRB is covalently crosslinked. Representative of 3 independent experiments. **i**, **j** Flow cytometry analysis of the CD69 expression of the SynVAC-pMHC cocultured with sorted ESO-T cells for 48 h ($N = 3$), which indicates that high viscoelasticity SynVAC-pMHC better activates ESO-T cells at the early time point. N represents the number of biologically independent samples. In (**b**, **c**, **j**), data represent mean ± s.e.m.; and a one-way ANOVA determined significance. (ns not significant, $^{*}P < 0.05$, $^{**}P < 0.01$, $^{***}P < 0.001$; $^{****}P < 0.0001$). We have provided the source data in the Excel file.

To further assess the functional outcome of these early interactions, we measured the expression of the early activation marker CD69 following short-term coculture (Fig. 1i). CD69 is rapidly upregulated upon TCR engagement and serves as a sensitive indicator of proximal signaling events within the first few hours of antigen recognition. Compared to MRBs and SRBs, which possess reduced viscoelasticity, FRBs induced markedly higher levels of CD69 expression (Fig. 1j). This enhanced activation suggests that both the mechanical properties and the biochemical ligand presentation of FRBs synergize to potentiate early T cell signaling.

Together, these results indicate that the viscoelastic nature of FRBs not only facilitates stable synapse formation but also promotes more efficient initiation of T cell activation.

Antigen-specific expansion of human primary PBMCs by SynVAC-pMHC

To investigate whether mechanical relaxation of SynVAC-pMHC regulates antigen-specific T cell responses, we performed in vitro expansion experiments using SynVAC-pMHC with distinct viscoelastic relaxation times. PBMCs from HLA-A2-positive donors were activated using FRB, MRB, SRB, or moDCs at a 1:1 ratio, followed by restimulation on day 7 and functional assessment on day 14 (Fig. 2a). Consistent with prior results, FACS analysis showed that FRBs drove significantly higher ESO-T cell frequency (Fig. 2b, c) and expansion (Fig. 2d) than MRBs or SRBs on day 14, suggesting that the presentation of pMHC with fast relaxation promotes T cell proliferation and/or survival. We further compared SynVAC-pMHC with an artificial APC platform based on the K562 cell line expressing ESO-HLA, along with the co-stimulatory molecules CD80, CD83, and 4-1BBL, which is a modest and insignificant increase to MRB and SRB, but significantly less than FRB (Supplementary Fig. 3).

To assess functional cytotoxicity, ESO-T cells expanded under each condition were co-cultured with HLA-A2/NY-ESO-1 positive melanoma (A375-FG) or ovarian (OVCAR3-FG) tumor targets for 24 h (Fig. 2e). The results showed superior tumor-killing efficiency in the FRB group (Fig. 2f, g). Cytokine analysis via ELISA further confirmed this trend: FRB-expanded T cells secreted higher levels of IFN-γ, TNF-α, and IL-2 (Fig. 2h–j), suggesting enhanced killing capability. Furthermore, T cell and tumor organoid co-culture indicated a superior infiltration capability, with the FRB resulting in the greatest T cell infiltration into the organoids compared to MRB, SRB, and control conditions (Fig. 2k, l). These results demonstrate that modulating the viscoelastic properties of SynVAC-pMHC can substantially affect antigen-specific T cell expansion, effector function, and cytokine secretion at the whole-culture level.

To further determine whether these differences reflected changes in cytokine production within the antigen-specific T cell population, we performed intracellular cytokine staining followed by flow cytometry after tumor killing assays, with the analysis pre-gated on ESO-T cells. In this per-cell analysis, FRB-stimulated ESO-T cells showed a modest increase in the frequency of IFN-γ-producing cells compared with MRB-, SRB-, and moDC-stimulated cells (Supplementary Fig. 4). TNF-α production showed a smaller increase, reaching significance only when compared with moDC, whereas IL-2 production was largely comparable across groups. Together, these data suggest that FRB stimulation primarily enhances ESO-T cell expansion at the population level, while also modestly increasing effector cytokine production within the antigen-specific T cell compartment.

scRNA-seq analysis of expanded T cell populations

To examine how mechanical relaxation of SynVAC-pMHC affects long-term T cell differentiation, we performed single-cell RNA sequencing on ESO-T cells expanded by FRB and SRB, alongside moDCs as the benchmark for antigen-specific activation, using the 10× Genomics platform at day 14. Following alignment with CellRanger (V9.0.0), downstream analysis was performed in Seurat (v4.3.0). To ensure that UMAP's two-dimensional (2D) embeddings reliably inform the similarities among cell clusters, scDEED (v0.1.0) was used to optimize the UMAP hyperparameters and minimize the number of dubious cell embeddings[31]. The UMAP visualization revealed eight distinct clusters (Fig. 3a), which were annotated based on gene expression profiles in stemness, proliferation, residency, effector, and exhaustion (Fig. 3b).

As shown in Fig. 3b, FRB-expanded ESO-T cells had more T memory stem (cluster 1 in 3a) and T central memory (cluster 2 in 3a) subsets. In contrast, SRB- and moDC-expanded cells exhibited higher proportions of exhausted cells (cluster 7, 8) and terminally differentiated T cells (cluster 5) (Supplementary Fig. 5). Heatmap projections of CCR7, TCF7, and SELL expression further confirmed elevated stemness-related gene expression in FRB-expanded cells (Fig. 3c and Supplementary Fig. 6), along with decreased expression of exhaustion-related markers, including PDCD1, LAG3, and TIGIT. Moreover, a Trm-like cluster enrichment in both SynVAC-pMHC-expanded groups compared with moDC-expanded cells (Supplementary Fig. 5), which are often associated with local persistence, rapid recall responses, and tumor-site immune surveillance[32].

Gene ontology analysis using the fgsea packages[33] and Gene Ontology Biological Processes (GOBP)[34,35] revealed that cell proliferation-related pathways (e.g., Cell Cycle, Cell Cycle Process) were significantly upregulated in FRB-expanded cells (Fig. 3d), corroborating their robust expansion profile. Using the Pathway Interaction Database, we found an increased expression of TCR pathway-related genes in the FRB group (Supplementary Fig. 7a). We also observed upregulation of OXPHOS-related genes and downregulation of glycolysis-related genes in the FRB group, consistent with the increased percentage of memory stem cells (Supplementary Fig. 7b, c).

Consistent with the transcriptional findings, flow cytometry analysis showed an increased frequency of memory-associated ESO-T cell populations in the FRB-expanded group (Fig. 3e). FRB-expanded cells also exhibited a higher proportion of Trm-like cells and a reduced exhausted phenotype, as indicated by CXCR6, PD-1, and TIM-3 expression (Fig. 3f).

Overall, our single-cell analysis demonstrates that the mechanical environment is a critical determinant of T cell fate. The FRB-expanded T cells retained stemness characteristics, showed robust proliferative capacity, and avoided the terminal exhaustion pathways observed in both the SRB and moDC groups. These integrated findings confirm that using SynVAC-pMHC (FRB) with high viscoelasticity can generate antigen-specific T cells optimized for persistence.

Intracellular signaling of ESO-T cells activated by SynVAC-pMHC

To understand how high and low viscoelasticity influences TCR proximal signaling, we examined the formation of the immunological synapse, a critical structure for T cell activation[36,37]. At 15 min post-stimulation, SRB induced a more prominent initial immunological synapse compared to FRB (Fig. 4a). At 30 and 60 min, FRB-mediated synapses remained, while SRB-induced synapses disappeared (Fig. 4a). These findings indicate that FRB promotes more stable formation of the immunological synapse than SRB, which likely enhances T cell activation. with significant increase in actin recruitment but not LFA-1 due to the lack of differential activation of LFA-1 or the absence of LFA-1 ligands such as ICAM-1 (Supplementary Fig. 8). These results suggest that viscoelasticity regulates the dynamics and stability of immunological synapse assembly.

To evaluate early T cell activation responses, we performed intracellular staining for phosphorylation of TCR downstream signaling markers at 30 min post-activation, which showed a significant increase in the FRB group (Supplementary Fig. 9). We also conducted Western Blotting analysis of ESO-T cells 60 min post-activation. The results showed that phosphorylation of IKBα, NFκB, and c-Jun was enhanced in the FRB-activated group (Supplementary Fig. 10a),

https://doi.org/10.1038/s41467-026-78131-6

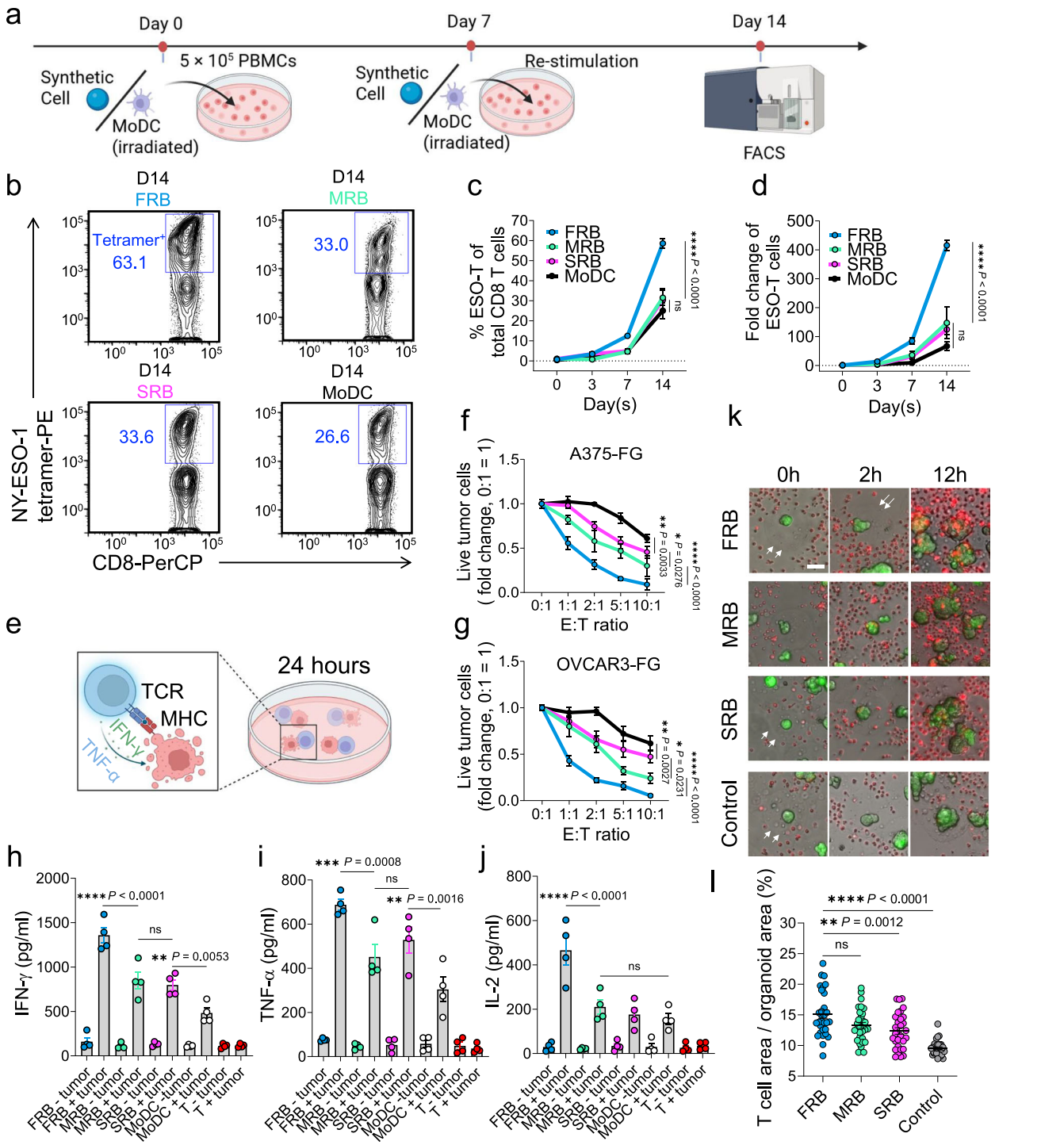


Fig. 2 | In vitro expansion and functional characterization of TCR-T cells by SynVAC-pMHC. a Experimental workflow: PBMCs were stimulated with irradiated moDCs or SynVAC-pMHC (FRB, MRB, or SRB) at day 0 with restimulation on day 7. The media was changed 2 days after the addition of SynVAC-pMHC to remove the synthetic cells. The cell culture on day 14 was used for the following FACS analysis. Created in BioRender. Liu, Z. (2026) https://BioRender.com/gbm0d13. **b** Representative flow cytometry analysis of the ESO-T percentage of cells expanded by different SynVAC-pMHC or moDCs. Representative of 3 independent experiments. **c**, **d** SynVAC-pMHC, particularly FRBs, promoted stronger expansion of ESO-T cells over time, as measured by tetramer staining and cell number measurement ($N = 3$). N represents the number of biologically independent samples. **e** Schematic representation of the in vitro tumor killing assay, where T cells and tumor cells were cocultured for 24 h. Created in BioRender. Liu, Z. (2026) https://BioRender.com/571sc88. **f**, **g** FRB-expanded ESO-T cells demonstrated superior tumor killing against ESO-T cell + A375-FG (melanoma) and OVCAR3-FG (ovarian) tumor targets across multiple effector-to-target (E: T) ratios ($N = 4$). N represents the number of biologically independent samples. **h**–**j** Cytokine analysis showed increased production of IFN-γ, TNF-α, and IL-2 from FRB-stimulated ESO-T cells following co-culture with tumor cells ($N = 4$). N represents the number of biologically independent samples. **k** Representative images of A375-FG tumor organoid cocultured with ESO-T cells at 0, 2, and 12 h. E:T ratio = 5:1. Scale bar, 70 μm. Representative of 3 independent experiments. **l** Quantitative analysis of the organoid infiltration index, which is calculated by the area of T cells in an organoid divided by the area of the organoid ($N = 30$). In (**c**, **d**, **f**–**j**, **l**) data represent mean ± s.e.m.; and significance was determined by two-way ANOVA (**c**, **d**) or one-way ANOVA (**f**–**j**, **l**) (ns not significant, $^{*}P < 0.05$, $^{**}P < 0.01$, $^{***}P < 0.001$; $^{****}P < 0.0001$). We have provided the source data in the Excel file.

https://doi.org/10.1038/s41467-026-78131-6

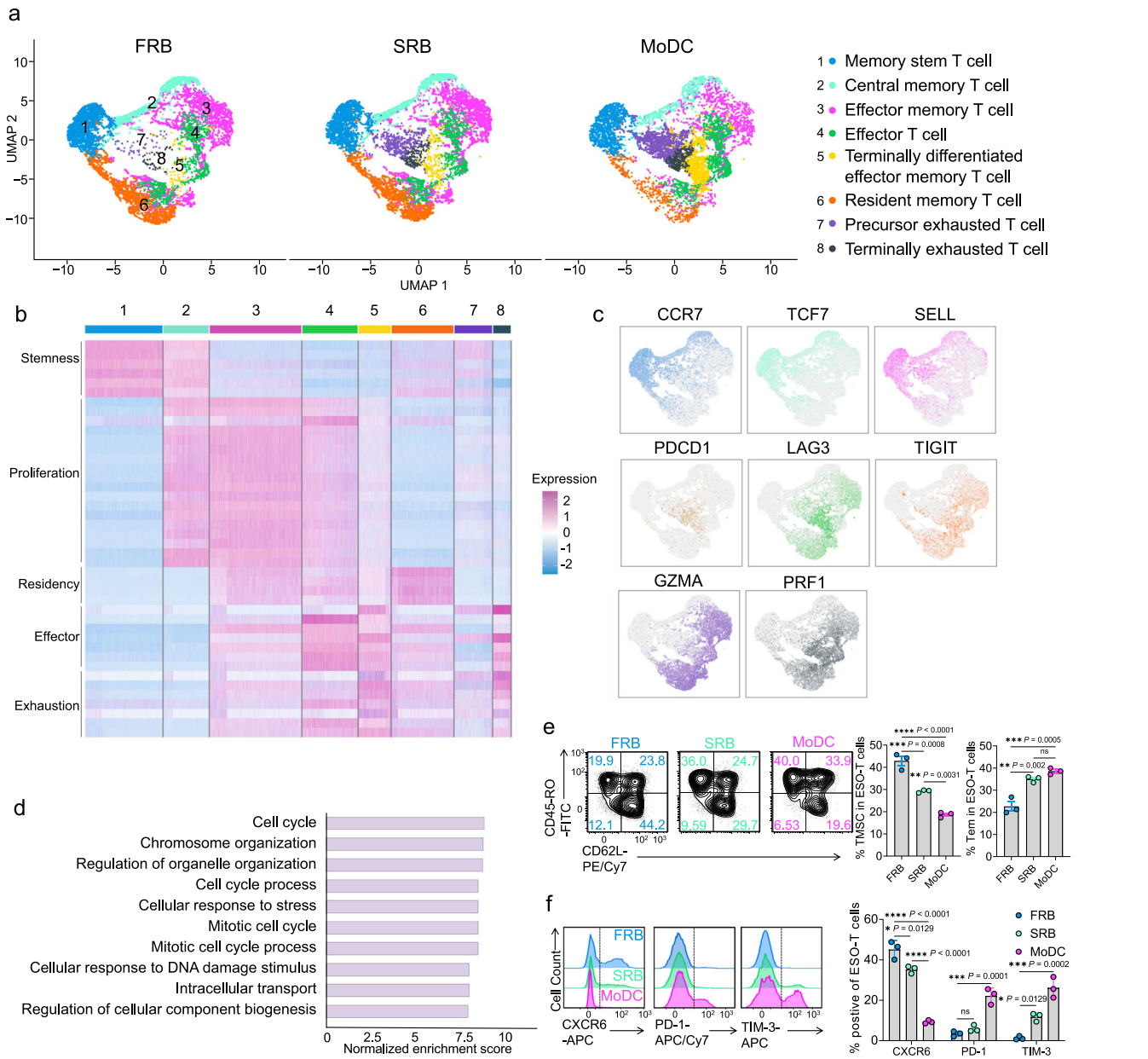


Fig. 3 | Single-cell RNA sequencing analysis of ESO-T cells expanded by SynVAC-pMHC or moDCs at Day 14. a UMAP clustering of ESO-T cells identifies distinct functional populations, including memory stem T cell, central memory T cell, effector memory T cell, effector T cell, terminally differentiated T cell, resident memory T cell, precursor exhausted T cell, and terminally exhausted T cell. **b** Gene lists that are used to identify different clusters in (**a**), including stemness, proliferation, residency, effector, and exhaustion. **c** Expression patterns of stemness marker genes (CCR7, TCF7, SELL), exhaustion marker genes (PDCD1, LAG3, TIGIT), and effector marker genes (GZMA and PRF1) projected onto UMAP space, highlighting transcriptional features that define distinct T cell subsets. **d** Gene set enrichment analysis (GSEA) of the FRB group using the Gene Ontology Biological Process (GOBP) database, highlighting pathways related to cell division, was significantly upregulated in the FRB-expanded ESO-T cells. **e** Representative flow cytometry plots of expanded ESO-T cells and quantification of Tscm and Tem cell frequencies in the FRB, SRB, and moDC groups ($N = 3$). Representative of 3 independent experiments. **f** Representative flow cytometry histograms of CXCR6, PD-1, and TIM-3 expression in expanded ESO-T cells and quantification of CXCR6-, PD-1-, and TIM-3-positive cell frequencies in the FRB, SRB, and moDC groups ($N = 3$). Representative of 3 independent experiments. In (**a**–**d**), scRNA-seq was performed on PBMCs from one donor, with one sample analyzed per condition. A total of 34538 cells (FRB 11642 cells; SRB 11398 cells; MoDC 11498 cells) passed quality control and were included in the analysis. In (**e** and **f**), data represent mean ± s.e.m.; and significance was determined by one-way ANOVA (NS not significant, $^{*}P < 0.05$, $^{**}P < 0.01$, $^{***}P < 0.001$; $^{****}P < 0.0001$). We have provided the source data in the Excel file.

suggesting increased activation of NFκB and AP-1. To further validate our results, we performed bulk RNA sequencing on ESO-T cells at 6 and 24 h after stimulation with SynVAC-pMHC (FRB versus SRB). Reads were aligned using STAR (v2.7.11b) and analyzed with DESeq2[38], with Clipper being used to control the false discovery rate when comparing differentially expressed genes between FRB and SRB[39]. Initial PCA analysis indicated that FRB, SRB, and the control group are in different locations on the PC1 and PC2 axes, suggesting distinct transcriptomes at both 6 and 24 h post-activation (Supplementary Fig. 10b).

Consistently, Gene Set Enrichment Analysis (GSEA), performed using the Pathway Interaction Database and 6-h post-activation RNA-seq data[33,40], revealed that key TCR downstream pathways—including NFAT, NF-κB, AP-1, and CD8 signaling—were enriched in FRB-activated cells (Fig. 4b). We also assessed the top upregulated and

https://doi.org/10.1038/s41467-026-78131-6

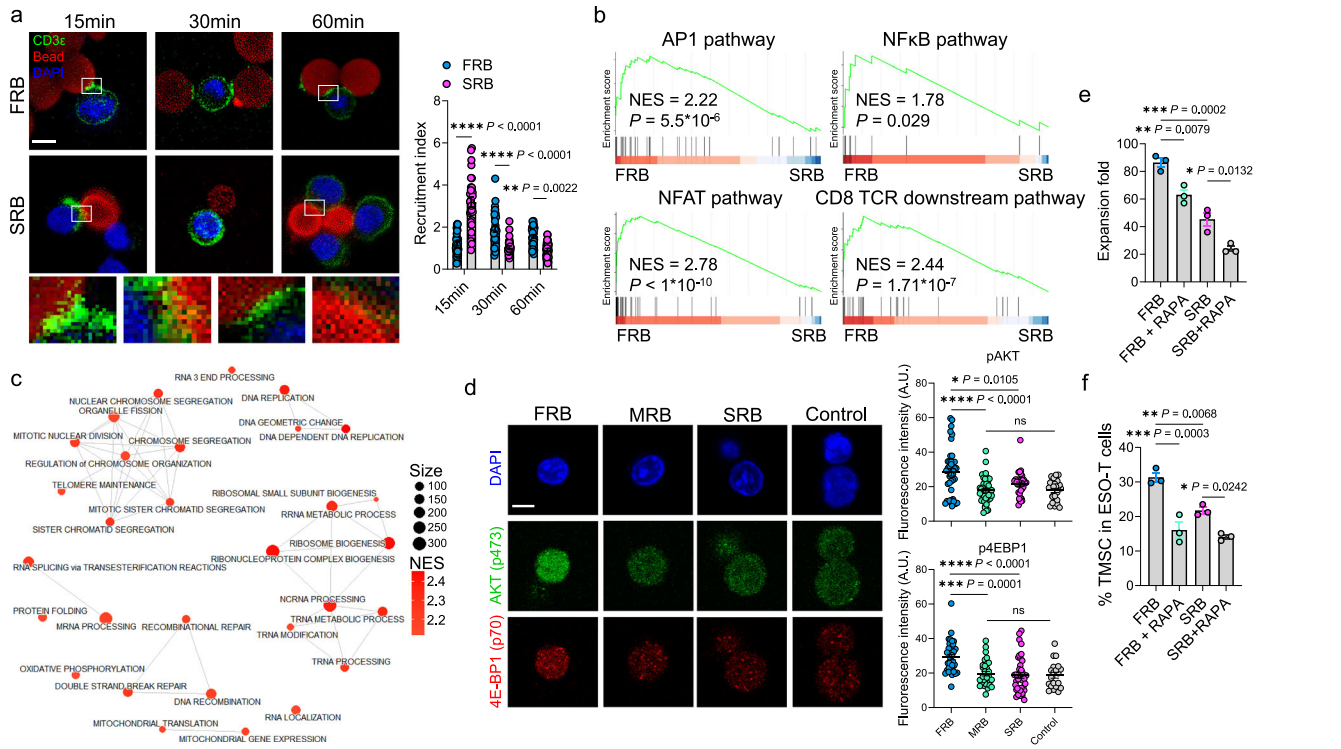


Fig. 4 | FRB induces stronger early T cell activation signals and enhances mTOR-mediated expansion and TMSC formation. a Confocal imaging of ESO-T cells forming immunological synapses with FRB or SRB at 15, 30, and 60 min post-activation. FRB showed stronger interaction with ESO-T cells as evidenced by a higher CD3e recruitment index ($N = 30$). Representative of 3 independent experiments. Scale bar: 5 µm. **b** Gene set enrichment analysis (GSEA) result of bulk RNA sequencing data from FRB and SRB-activated ESO-T cells at 6 h post-activation ($N = 4$), showing enhanced early T cell activation signals in the FRB group. The PID dataset from the Molecular Signatures Database was used for GSEA. *P*-value is calculated using the R package function. **c** Enrichment Map plot of bulk RNA sequencing data from FRB and SRB-activated ESO-T cells at 24 h post-activation ($N = 4$), showing enhanced cell division and metabolism in the FRB group. Normalized enrichment score (NES) was calculated using GSEA of the gene ontology: biological process (GO: BP) dataset from the Molecular Signatures Database. **d** Confocal imaging of the phosphorylated AKT and 4E-BP1 in ESO-T cells activated for 1 h, which are downstream targets of mTORc2 and mTORc1, respectively, showing enhanced mTOR signals for the FRB group. Scale bar: 5 µm. The number of cells analyzed for control group ranged from 20 to 26. The number of cells analyzed for treatment group ranged from 30 to 45. Representative of 3 independent experiments. **e** The expansion fold of ESO-T cells cocultured with FRB or SRB with or without the addition of 100 nM rapamycin (RAPA) during the coculture period, which shows that mTOR signaling is involved in T cell proliferation. Representative of 3 independent experiments. **f** The T memory stem cell (TMSC) percentage of ESO-T cells cocultured with FRB or SRB in the absence or presence of 100 nM rapamycin (RAPA) during the coculture period, which shows the role of mTOR signaling in TMSC generation. Representative of 3 independent experiments. In (**a**, **d**–**f**), data represent mean ± s.e.m.; and significance was determined by one-way ANOVA (NS not significant, $^*P < 0.05$, $^{**}P < 0.01$, $^{***}P < 0.001$; $^{****}P < 0.0001$). We have provided the source data in the Excel file.

downregulated genes between the FRB and SRB groups. We found that the SRB expression pattern falls between those of the FRB and control groups (Supplementary Fig. 10c). These results suggest that FRB more effectively activates ESO-T cells at both the transcriptional and early phosphorylation signaling levels.

Following the enhanced signals, at 24 h post-activation, FRB-stimulated cells showed an upregulation of genes associated with metabolism (e.g., VDAC1, SCD, HK2) and cell cycle progression (e.g., NSD2, TYMS, CDK2), alongside downregulation of naïve T cell–associated genes (e.g., TCF7, IL7R, KLF2) (Supplementary Fig. 10d). GSEA analysis with the hallmark gene sets further confirmed the upregulation of glycolysis and OXPHOS-related genes in the FRB group (Supplementary Fig. 10f). Pathway interaction maps based on GOBP showed that FRB-stimulated cells were enriched for mitochondrial metabolism, OXPHOS, and ribosome biogenesis, reflecting a metabolically active and proliferative state (Fig. 4c). Additional upregulated pathways included mRNA processing, DNA replication and repair, and telomere maintenance, suggesting coordinated activation of gene-expression and proliferative programs that support early T cell activation. Consistently, the most enriched pathways at 24 h in the FRB group include DNA repair and proliferation pathways (Supplementary Fig. 10g), such as ATR, FANCONI, and PLK1 signaling. These results indicated a heightened proliferative potential in the high-viscoelasticity SynVAC-pMHC group, aligning with previously reported findings supporting T cell expansion.

Costimulatory molecules such as CD28 are also a critical component of the immunological synapses, which have been shown to enhance the mTOR activity in T cells[41,42]. The mTOR pathway is a central regulator of T cell metabolism. Among its two functional complexes, mTORC1 promotes glycolytic metabolism, whereas mTORC2 supports mitochondrial oxidative metabolism, including OXPHOS[43,44]. To assess whether the more persistent FRB-induced synapses corresponded to stronger mTOR activity, we measured phosphorylation of 4E-BP1 and AKT at Ser473, commonly used readouts of mTORC1- and mTORC2-associated activity, respectively. FRB-activated T cells exhibited higher levels of both p-4EBP1 and p-AKT compared to MRB or SRB conditions (Fig. 4d). Transcription factor target analysis of the RNA sequencing results also indicated higher activity of mTOR-regulated factors in the FRB-treated group (Supplementary Fig. 10e).

To determine whether mTOR signaling mediated the enhanced T cell stemness, we applied rapamycin during the coculture period, which inhibited both mTORC1 and mTORC2 activity (Supplementary Fig. 10h). This leads to impaired T cell metabolism (Supplementary

https://doi.org/10.1038/s41467-026-78131-6

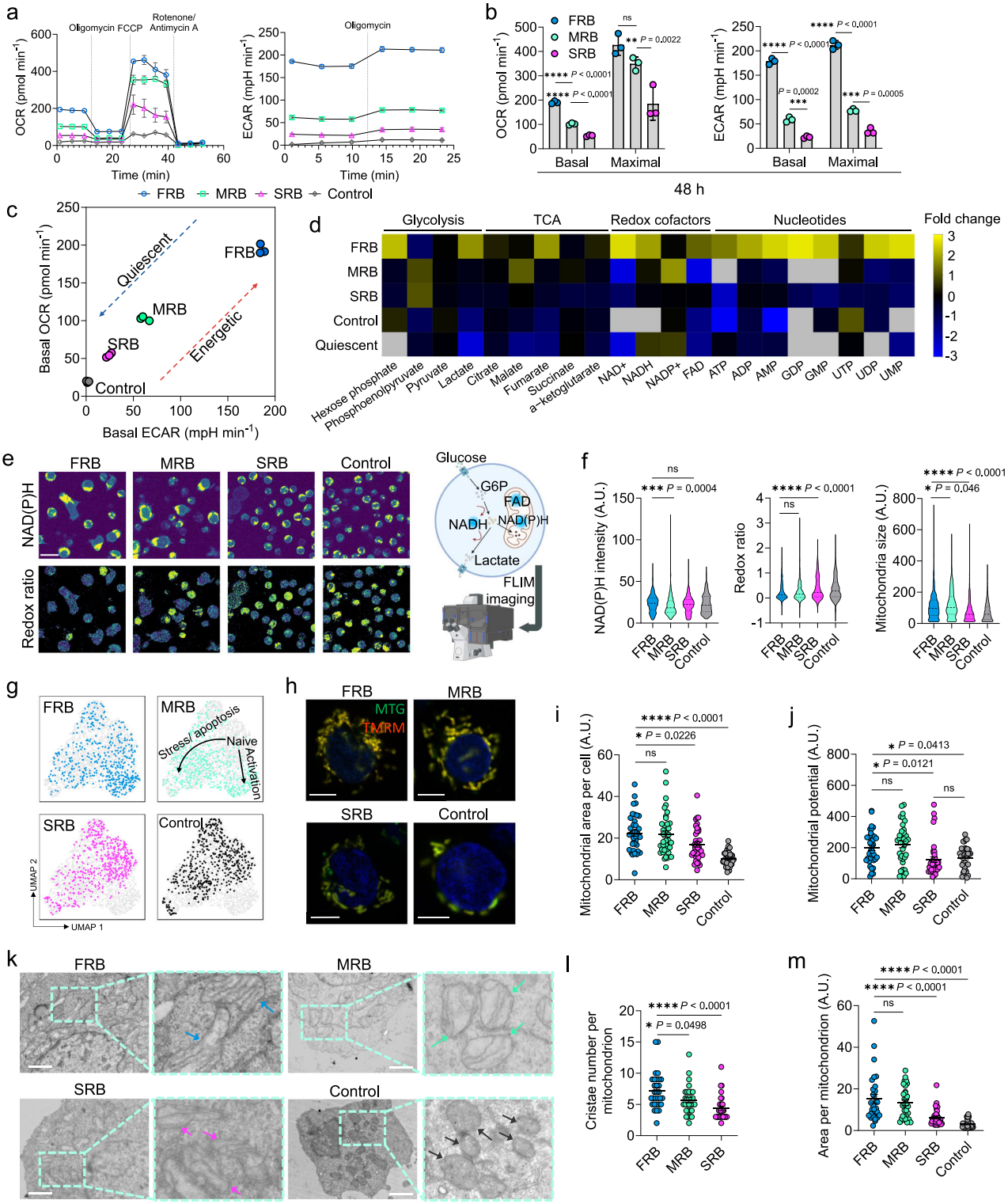


Fig. 10i), reduced T cell expansion, and reduced generation of TMSCs (Fig. 4e, f). These results demonstrate that mTOR signaling is critical for the FRB-induced enhancement of T cell activation, proliferation, and differentiation.

Metabolic reprogramming of ESO-T cells following activation by SynVAC-pMHC

At the transcriptional level, GSEA of the 24-h sequencing showed enriched OXPHOS and glycolysis-related genes (Supplementary Fig. 10f). To further validate whether FRB-induced activation enhances T cell bioenergetics, we performed a series of analyses on the metabolic activity of ESO-T cells stimulated with FRBs 48 h post-activation.

At 48 h post-activation, we observed an increase in cell size in the FRB group compared to other formulations of SynVAC-pMHC (Supplementary Fig. 11a), which is often related to a metabolic switch to glycolysis to support T cell growth and proliferation[45,46]. To quantify the metabolic rate of SynVAC-pMHC-activated cells, the Seahorse XF assay was used to measure OXPHOS and glycolysis rates (Fig. 5a). FRB-stimulated ESO-T cells exhibited significantly higher basal and maximal oxygen consumption rates (OCR) and elevated extracellular

Fig. 5 | FRB promotes early metabolic activation in ESO-T cells. a Seahorse analysis of oxygen consumption rate (OCR, left) and extracellular acidification rate (ECAR, right) in ESO-T cells 48 h after activation by FRB, MRB, or SRB ($N = 3$). *N* represents the number of biologically independent samples. **b** Quantification of basal and maximal OCR (left) and ECAR (right) showing enhanced mitochondrial respiration and glycolytic activity in FRB-stimulated cells ($N = 3$). *N* represents the number of biologically independent samples. **c** Basal OCR and ECAR of ESO-T cells expanded by different SynVAC-pMHC, showing a more energetic metabolic profile of the FRB-activated ESO-T cells ($N = 3$). **d** Heatmap showing the log2 fold change of key intracellular metabolites, grouped by pathway (Glycolysis, TCA Cycle, Redox cofactors, Nucleotides), comparing FRB, MRB, SRB, Control (IL-2 only), and Quiescent groups ($N = 3$). Fold change is calculated by dividing the raw value by the row-wise mean. **e** Fluorescence Lifetime Imaging Microscopy (FLIM) images of ESO-T cells activated by different SynVAC-pMHC. The redox ratio is calculated as the fluorescent intensity of FAD divided by the fluorescent intensity of NAD(P)H. Representative of 3 independent experiments. Scale bar: 20 μm. Illustration created in BioRender. Liu, Z. (2026) https://BioRender.com/e9yu5ny. **f** Quantification of (**e**) and mitochondrial size, showing FRB promotes NAD(P)H signal and mitochondrial size growth. **g** 2D metabolic state mapping of individual cells using FLIM-derived features shows distinct clustering of FRB-stimulated cells in an activated metabolic region. At the same time, SRB and control groups remain in lower-activity regions. The schematic on the right shows the mechanism of FLIM imaging, in which the autofluorescence and fluorescence lifetimes of FAD and NAD(P)H are detected by the microscope. **h** Representative confocal imaging of mitochondria structure (Mitotracker Green) and mitochondrial potential (Tetramethylrhodamine methyl ester [TMRM]) staining. Scale bar: 5 μm. Representative of 3 independent experiments. **i** Quantification of mitochondrial area per cell in (**h**) ($N = 38$). Representative of 3 independent experiments. **j** Quantification of mitochondrial potential in (**h**) ($N = 38$). Representative of 3 independent experiments. **k** Representative images acquired by transmission electron microscope (TEM) of ESO-T cells activated by FRB, MRB, SRB, and control. Arrows indicate mitochondria. Scale bar: 1 μm. Representative of 3 independent experiments. **l** Quantification of the cristae number per mitochondrion ($N = 30$). Representative of 3 independent experiments. **m** Quantification of the mitochondria size ($N = 30$). Representative of 3 independent experiments. In (**a**, **b**, **f**, **i**, **j**, **l**, **m**), data represent mean ± s.e.m.; and a one-way ANOVA determined significance (ns not significant, $^{*}P < 0.05$, $^{**}P < 0.01$, $^{***}P < 0.001$; $^{****}P < 0.0001$). We have provided the source data in the Excel file.

acidification rates (ECAR) compared to MRB- and SRB-stimulated cells (Fig. 5b), indicating enhanced mitochondrial respiration and aerobic glycolysis (Fig. 5c). This phenomenon was further confirmed by using cells from other donors, showing a more energetic metabolism profile in the FRB group (Supplementary Fig. 11b–d). Consistent with this enhanced early bioenergetic state, FRB stimulation also increased lipid uptake, including neutral lipids and long-chain fatty acids, further indicating elevated nutrient acquisition to support T cell activation and growth (Supplementary Fig. 12). LC-MS metabolomics further revealed increased levels of intracellular lactate, TCA metabolites, redox cofactors, and nucleotides in FRB-expanded cells, consistent with higher energy turnover (Fig. 5d and Supplementary Fig. 11e). However, the metabolic difference became less apparent by day 5 (Supplementary Figs. 12 and 13), suggesting that FRB primarily accelerates early metabolic activation rather than maintaining a persistent bioenergetic divergence.

To visualize metabolic activity at the single-cell level, label-free fluorescence lifetime imaging microscopy (FLIM) was used to measure NAD(P)H intensity and optical redox ratios (i.e., FAD/NAD(P)H), following a previously established label-free optical metabolic imaging framework for resolving cell-state transitions at single-cell resolution[47,48]. FRB-activated T cells displayed elevated NAD(P)H signal and lower redox ratios, indicative of a metabolically active state with enhanced biosynthetic potential and upregulation of glycolysis (Fig. 5e, f). Consistently, we observed an increased cell size in the FRB group during imaging (Supplementary Fig. 11f). We then integrated multiple FLIM-derived metabolic features—including cell morphology, and NAD(P)H lifetimes, intensity, redox ratio, and subcellular distribution—into a 2D metabolic activation map to characterize T cell phenotype (Supplementary Fig. 11g). In this analysis, FRB-stimulated cells clustered more tightly in a region representing high mitochondrial activity, whereas SRB- and control-stimulated cells were more dispersed and occupied regions associated with lower metabolic activity (Fig. 5g). This suggests that FRB stimulation elicits a more uniform and robust metabolic activation program at the single-cell level, whereas MRB- and SRB-activated cells exhibit less metabolic activity.

Mitochondrial fusion, fission, and biogenesis have also been shown to regulate T cell activation, survival, memory formation, and effector differentiation[49]. To comprehensively assess the metabolic state of the T cells, we evaluated mitochondrial fitness using confocal imaging and MitoTracker Green (for mitochondrial mass) and TMRM (for membrane potential) staining (Fig. 5h). The results indicated that FRB-expanded T cells exhibited increased mitochondrial mass (Fig. 5i) and a higher mitochondrial membrane potential (Fig. 5j) compared to the SRB group, suggesting enhanced mitochondrial activity. To further characterize these changes, we used transmission electron microscopy (TEM) to examine individual mitochondrial structures (Fig. 5k). TEM images revealed that mitochondria in the FRB group had a greater cristae density (Fig. 5l) and were significantly larger (Fig. 5m), both of which are critical for maximizing the surface area available for OXPHOS. These results indicate that FRB-activated ESO-T cells have healthier and more functionally robust mitochondria.

Together, these findings support the hypothesis that viscoelasticity is a key regulator of early T cell metabolic programming, with rapid stress relaxation enhancing mitochondrial function, OXPHOS, and glycolytic activity, thereby promoting a more active metabolic state. Furthermore, we found that MRB- and SRB-activated cells are similar in OXPHOS and glycolysis rates, suggesting an optimal viscoelasticity range for T cell metabolic reprogramming.

ESO-T cells expanded with FRB demonstrate superior antitumor capacity in multiple solid tumor xenograft mouse models

To evaluate the translational potential of viscoelastic stimulation, we selected the FRB, which exhibited optimal T cell activation and metabolic fitness in vitro. We compared it with the moDC group, the current gold standard for antigen-specific T cell expansion. We assessed the in vivo antitumor efficacy of ESO-T cells generated under these two conditions using two solid tumor xenograft models: the OVCAR3-FG human ovarian cancer model and the A375-FG human melanoma model. In the OVCAR3-FG model, tumor cells were injected intraperitoneally (i.p.) into NSG mice to establish a peritoneal tumor burden, mimicking a localized peritoneal disease setting (Fig. 6a). In contrast, A375-FG cells were injected subcutaneously (s.c.) to form solid tumors, allowing assessment of the tumor-homing capacity and antitumor efficacy of ESO-T cells in a solid tumor context (Fig. 6h).

In the OVCAR3-FG humanized mouse model, ESO-T cells expanded by using FRB or moDCs suppressed tumor growth (Fig. 6b, c). However, ESO-T cells generated with FRB exhibited markedly superior antitumor activity, leading to complete tumor elimination in all experimental mice (Fig. 6b, c). Biodistribution and phenotypic analyses of ESO-T cells across multiple organs revealed enhanced in vivo persistence, expansion, and preferential accumulation at the peritoneal (tumor site) (Fig. 6d, f). Furthermore, these cells showed enrichment of ESO-specific (ESO^{+}) T cells, suggesting antigen-specific expansion following tumor encounter (Fig. 6e, g). They also expressed elevated levels of T cell activation markers (i.e., PD-1) (Fig. 6e, g).

In the A375-FG human melanoma xenograft model, the two types of ESO-T cells were also evaluated (Fig. 6h). Consistent with the results from the OVCAR3-FG model, ESO-T cells generated with FRB achieved

https://doi.org/10.1038/s41467-026-78131-6

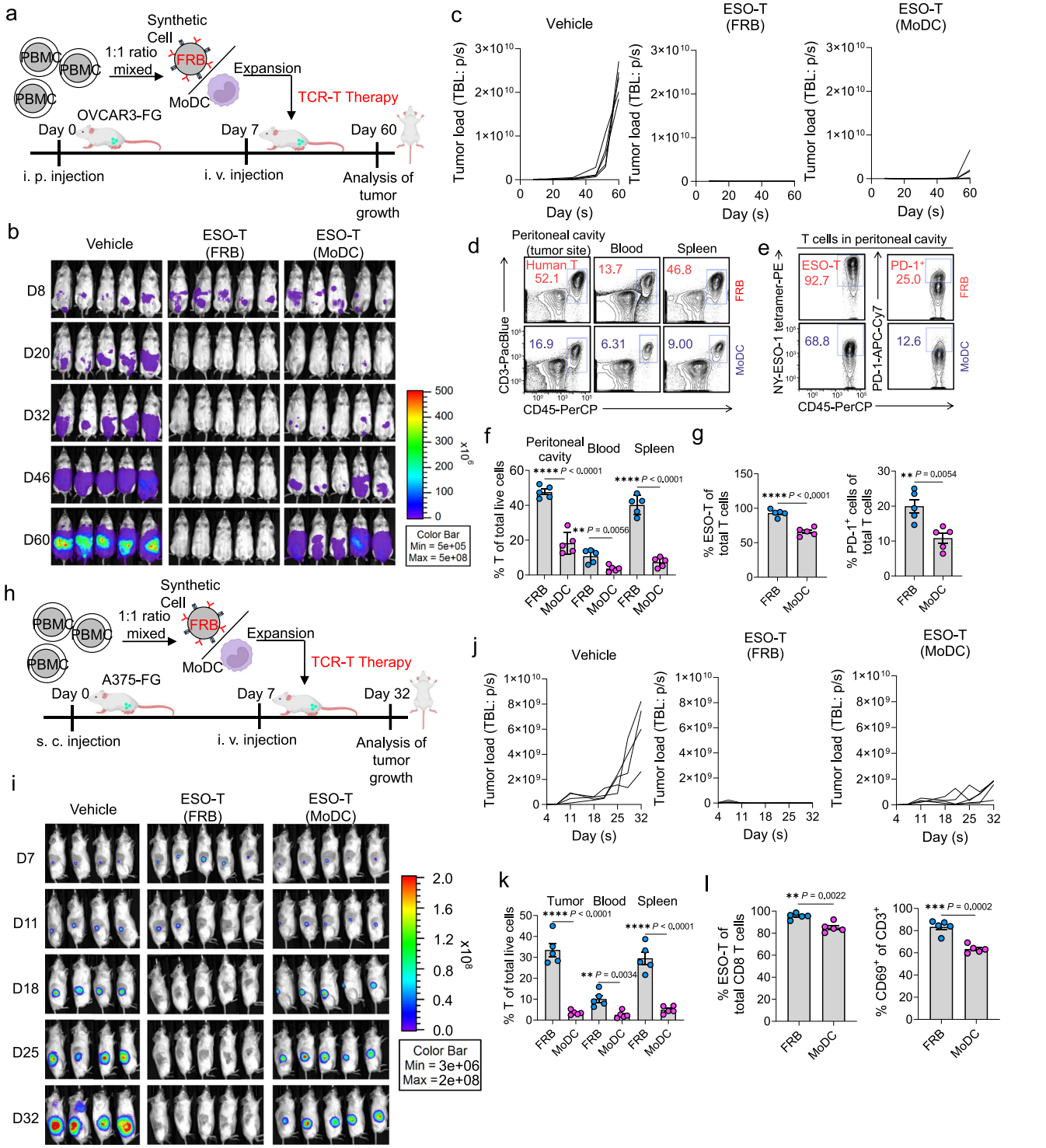


Fig. 6 | SynVAC-pMHC-expanded TCR-T cells exhibit enhanced antitumor efficacy and persistence in an ovarian cancer model and a melanoma model. **a** Experimental design of the ovarian cancer model. Partially created in BioRender. Yang, Y. (2026) https://BioRender.com/pk28pj7. **b** BLI images showing the presence of ovarian cancer cells in experimental mice over time. **c** Quantification of (**b**) ($N = 5$). **d** Representative flow cytometry results of the frequency of human T cells in the peritoneal cavity, blood, and spleen at day 60 ($N = 5$). Representative of 3 independent experiments. **e** Representative flow cytometry results of the frequency of ESO-T cells and PD-1$^+$ T cells in the peritoneal cavity at day 60 ($N = 5$). Representative of 3 independent experiments. **f** Quantification of (**d**) ($N = 5$). **g** Quantification of (**e**) ($N = 5$). **h** Experimental design of the melanoma model. Partially created in BioRender. Yang, Y. (2026) https://BioRender.com/pk28pj7. **i** BLI images showing the presence of melanoma cells in experimental mice over time ($N = 4$ for control group; $N = 5$ for experimental group). **j** Quantification of (**i**) ($N = 5$). **k** The frequency of human T cells in the tumor, blood, and spleen on day 32 ($N = 5$). **l** The frequency of ESO-T cells and CD69$^+$ T cells in the tumor on day 32 ($N = 5$). In (**f**, **g**, **k**, **l**), data represent mean ± s.e.m.; and a two-sided student's *t*-test determined significance (ns not significant, $^*P < 0.05$, $^{**}P < 0.01$, $^{***}P < 0.001$; $^{****}P < 0.0001$). We have provided the source data in the Excel file.

complete tumor elimination in all treated mice, demonstrating significantly higher efficacy compared to those expanded using moDCs (Fig. 6i, j). This superior antitumor activity may be attributed to enhanced tumor homing, greater in vivo expansion of ESO-T cells observed across multiple tissues (including blood and spleen) (Fig. 6k and Supplementary Fig. 14), and the enrichment of ESO-T cells with increased expression of the activation marker CD69 (Fig. 6l and Supplementary Fig. 15).

Collectively, these findings indicate that ESO-T cells expanded using FRB exhibit superior in vivo persistence, tumor-homing capacity, and antitumor efficacy, highlighting their promise as a potent cell product for solid-tumor immunotherapy.

Discussion

This study introduces SynVAC-pMHC as a synthetic, compositionally defined, and mechanically tunable antigen-presenting platform with potential utility for antigen-specific TCR-T cell manufacturing. SynVAC-pMHC enables precise control of the mechanical and biochemical signals required for T cell activation. We engineered these materials by manipulating the molecular weight and degree of crosslinking to create microparticles with a consistent stiffness of 10 kPa—similar to that of mature dendritic cells[50]—but with widely varying half-relaxation times, ranging from 10 to 2000 s. Importantly, the SynVAC-pMHC panel was designed to isolate stress relaxation from stiffness, two mechanical parameters that are often coupled in biomaterials but may be sensed differently by T cells. This distinction is critical because TCR engagement and immune synapse formation occur over time scales during which force dissipation, ligand mobility, and material remodeling may influence the duration and quality of TCR/CD28 signaling. This capability allows systematic exploration of how material viscoelasticity influences T cell activation and expansion, addressing a key limitation of existing biocompatible materials, which are typically highly elastic and poorly mimic the viscoelastic behavior of native antigen-presenting cells. One future study is that we did not directly measure TCR–pMHC on/off rates or force-dependent binding kinetics at the T cell–SynVAC interface, which would require specialized single-molecule or live-cell biophysical approaches such as membrane force probes, DNA tension sensors, optical tweezers, or high-resolution receptor–ligand imaging; this investigation can further define how SynVAC-pMHC stress relaxation regulates TCR engagement, immune synapse dynamics, and downstream T cell activation.

Under the conditions tested here, SynVAC-pMHC outperformed moDCs as a defined cellular comparator for antigen-specific T cell expansion. moDCs represent one of the current standards for TCR-T expansion but suffer from donor variability, phenotypic differences from naturally circulating DC subsets, and are typically generated using GM-CSF/IL-4, which may not recapitulate native APC function[6,7]. SynVAC-pMHC represents a consistent and scalable aAPC platform that provides a bottom-up approach to deliver well-defined signals, avoiding the mixed and undefined cues associated with moDCs, while uniquely integrating biomechanical modulation to drive metabolic reprogramming for more efficient TCR-T cell expansion. It will be interesting to directly benchmark SynVAC-pMHC against clinically used cGMP-compatible activation platforms, such as anti-CD3/CD28 bead-based systems with viral transduction or antigen-loaded PBMC-based expansion protocols. Such comparisons will be important for future translational development.

Since FRB stimulation increased both the ESO-T cell frequency and total expansion, the improved antitumor activity observed in the bulk-expanded product likely reflects a combination of antigen-specific T cell enrichment and qualitative changes in the resulting T cell population. Normalization to ESO-T frequency reduced the magnitude of functional differences in vitro; in addition, moDC-expanded cells could initially perform comparably to FRB-expanded cells in vivo, indicating that starting antigen-specific cell number contributes to the observed response (Supplementary Fig. 16). However, the later divergence in tumor control, together with the modest increase in per-cell IFN-γ production and the memory-like transcriptional features observed in ESO-T cells, suggests that FRB stimulation may also improve the durability and functional composition of the expanded product (Supplementary Fig. 16). We therefore interpret FRB-mediated benefits as arising from both population-level enrichment and changes in antigen-specific T cell state, while recognizing that future studies using sorted ESO-T cells will be required to fully separate these mechanisms from potential contributions of bystander T cells.

A central finding of this study is that the stress-relaxation behavior of the antigen-presenting interface acts upstream of T cell metabolic programming. Consistent with this interpretation, the NAD(P)H/FAD optical redox state provides an additional readout of activation-associated metabolic remodeling, reflecting changes in intracellular redox balance rather than a single metabolic pathway. This optical redox shift aligns with our Seahorse and metabolomics results, supporting the conclusion that FRB stimulation promotes a broader early bioenergetic activation state. Rather than producing a simple shift from OXPHOS to glycolysis, fast-relaxing SynVAC-pMHC induced a coordinated increase in both mitochondrial respiration and glycolytic activity, as shown by elevated basal and maximal OCR, increased ECAR, higher levels of TCA-cycle intermediates, lactate, redox cofactors, and nucleotide metabolites, and increased cell size. This metabolic profile is consistent with the bioenergetic demands of early $CD8^+$ T cell activation, during which T cells must simultaneously generate ATP, support biomass accumulation, and maintain biosynthetic flux for clonal expansion and effector differentiation. Thus, the FRB-induced metabolic state can be interpreted as a highly competent early activation program.

Additional metabolic measurements further support the interpretation that FRB promotes early metabolic fitness. FRB-stimulated cells showed increased uptake of neutral lipids and long- and medium-chain fatty acids, indicating enhanced lipid-handling capacity in addition to increased glucose-associated bioenergetics. Notably, the differences in Seahorse measurements and lipid uptake were more pronounced at early time points and became smaller by day 5. This suggests that SRB-stimulated cells are also activated and can enter the clonal expansion phase, but may do so with delayed or less efficient early metabolic priming compared with FRB-stimulated cells. Therefore, the key effect of FRB may occur during the early blasting phase, when metabolic remodeling is most closely linked to subsequent proliferative and differentiation trajectories.

Because cellular metabolism can regulate epigenetic remodeling through metabolite-dependent control of chromatin-modifying enzymes, we hypothesize that FRB-induced early metabolic reprogramming may help shape the epigenetic landscape of activated ESO-T cells[51–53]. In this model, the enhanced metabolic state induced during the blasting phase may act as an early imprinting event that influences later T cell fate decisions during clonal expansion. This could contribute to the increased TMSC/TCM-like populations and reduced terminal differentiation observed at day 14. However, elevated OCR, ECAR, mTOR-associated signaling, mitochondrial remodeling, and lipid uptake at early time points are also consistent with optimal activation, and direct causality between specific metabolic pathways, epigenetic remodeling, and memory-associated differentiation remains to be established. Future studies using pathway-specific perturbations of glycolysis, mitochondrial respiration, fatty acid oxidation, lipid uptake, mitochondrial biogenesis, and chromatin accessibility will be needed to define which metabolic programs are required for FRB-enhanced persistence and antitumor activity.

In conclusion, we reveal that the viscoelasticity of SynVAC-pMHC is a critical regulator of T cell metabolism and demonstrate its strong potential to enhance TCR T cell activation, expansion, and antitumor

efficacy. Our findings highlight the advantages of SynVAC-pMHC over conventional moDCs and support their utility as a next-generation platform to overcome key barriers in solid tumor immunotherapy, ultimately paving the way for more effective and durable TCR T-cell treatments in patients with ovarian cancer, melanoma, and beyond.

Methods

Study approval

This study was conducted in accordance with all relevant ethical regulations. All animal studies were approved by the UCLA Division of Laboratory Animal Medicine (ARC-2013-054). Healthy donor PBMCs were provided by the UCLA/CFAR Virology Core Laboratory in a de-identified manner and in accordance with applicable federal and state regulations (IRB-11-0443). Additional PBMCs and peripheral blood units were obtained from HemaCare from healthy donors who provided informed consent.

Fabrication of the synthetic cells with well-defined mechanical properties

Alginate viscoelastic microbeads were fabricated within the microfluidic device via a pH-induced internal gelation method, as previously described[54,55]. Polydimethylsiloxane (PDMS) prepolymer was combined with curing agent, cast onto the patterned silicon substrate and cured at 65 °C for 3 h. The resulting PDMS slab was cleaned with ethanol and bonded to glass by plasma treatment.

The aqueous formulation determined the bead relaxation properties. FRBs contained 3% VLVG alginate (70 kDa; NovaMatrix), 1% carboxymethyl cellulose (90 kDa; Sigma-Aldrich) and 20 mM Ca–EDTA in deionized water. MRBs contained 3% LVG alginate, 1% MVG alginate (both Sigma-Aldrich) and 20 mM Ca–EDTA in deionized water. The continuous phase comprised fluorocarbon oil (Novec 7500; 3 M), 1% surfactant (157 FSH; Krytox) and 0.5% acetic acid. Both phases were passed through 0.22-µm filters and delivered through separate device inlets using syringe pumps (Harvard Apparatus).

Droplets were collected in fluorocarbon oil containing 10% perfluoro-1-octanol (Sigma-Aldrich) and 0.2% acetic acid. HEPES buffer supplemented with 2 mM $CaCl_2$ (pH 7.2) was added, followed by centrifugation at $1500 \times g$ for 1.5 min to recover the aqueous bead suspension.

SRBs were generated by covalently crosslinking VLVG microbeads and subsequently removing calcium-mediated crosslinks. Beads were pelleted at $6000 \times g$ for 5 min and resuspended in MES–Ca buffer containing 1 mM $CaCl_2$ (pH 6). Following a second centrifugation, beads were incubated overnight in MES–Ca buffer containing EDC (50 mg ml^{-1}), HoBt (3.5 mg ml^{-1}), and AAD (0.52 mg ml^{-1}). Calcium was then chelated for 2 h using a solution containing 77 mM NaCl and 55 mM sodium citrate. Beads were washed with HEPES buffer containing 0.5% Tween-20 and stored at 4 °C.

Preparation of synthetic cells for T cell stimulation

Beads were functionalized using the tetrazine–TCO ligation strategy reported previously, with modifications for peptide–MHC presentation[54]. Four million beads were incubated for 1 h in 800 µl MES buffer containing 200 mM EDC hydrochloride and 200 mM sulfo-NHS. Activated beads were washed with 500 µl HEPES–CT buffer, comprising HEPES, 2 mM $CaCl_2$ and 0.5% Tween-20 at pH 7.2. TCO-PEG6-amine (Click Chemistry Tools) was added to a final concentration of 2 mM. The suspension was mixed overnight at room temperature on a roller. Unreacted reagent was removed by dialysis against HEPES–CT buffer using a 1000-kDa dialysis membrane (Spectrum Laboratories), with two or three buffer exchanges daily. HLA-A*02:01 tetramers presenting SLLMWITQV (NIH Tetramer Core Facility) were combined with anti-CD28 antibody (BioLegend, 302902) at a 1:1 molar ratio. The mixture was concentrated to 100 µl in HEPES buffer using an Amicon Ultra-2 centrifugal filter. Tetrazine-PEG5-NHS was added at a protein-to-reagent molar ratio of 1:5 and incubated for 30 min. Unreacted tetrazine reagent was removed using a spin column with five HEPES washes. The conjugates were mixed with an equal volume of glycerol and stored at −20 °C. Tetrazine-labelled proteins were coupled to TCO-functionalized beads. Protein input was adjusted for each formulation to obtain comparable ligand presentation. To confirm the conjugation of proteins on the bead surface, Rat anti-human HLA-A, B, C (BioRad), Alexa Fluor™ 647 goat anti-rat IgG, and Alexa Fluor™ 488 goat anti-mouse IgG (Invitrogen) were used to stain the beads. Confocal images were acquired with a Leica SP8-STED confocal microscope and analyzed in ImageJ.

Mechanical property and ligand density characterization of synthetic cells

Bulk hydrogels matching the aqueous formulations of the microbeads were prepared as discs measuring 8 mm in diameter and approximately 2 mm in thickness. For covalent gels, 3% VLVG alginate was initially crosslinked with calcium. Discs were equilibrated in MES buffer (pH 6) for 1 h and transferred to a stirred solution containing AAD and HoBt. Following overnight incubation at room temperature, discs were treated with sodium citrate buffer for 2 h. The gels were washed with deionized water and equilibrated in HEPES buffer for 24 h.

Oscillatory measurements were performed at room temperature using an Anton Paar rheometer. Each disc was positioned centrally between the measuring surfaces, with a gap of 1 mm. Frequency sweeps from 0.1 to 100 Hz were conducted at 1% strain to obtain the storage modulus (G′) and loss modulus (G″). At least three measurements were performed.

Compression testing was performed using a Chatillon TCD225 force measurement system. Before testing, discs were equilibrated in RPMI medium for 24 h. Samples were compressed at 1/120 mm s^{-1} for 30 s without prestress. The initial compressive modulus was calculated from the slope over the 5–10% strain interval. Displacement was then held fixed while force decay was recorded. The half-relaxation time was defined as the interval required for stress to reach 50% of its peak value. Identical procedures were applied to ionically and covalently crosslinked gels.

Relative HLA-associated fluorescence was measured by flow cytometry. For each formulation, 1×10^5 beads were labelled sequentially with rat anti-human HLA-A, B, C antibody and Alexa Fluor 647 goat anti-rat IgG. Washed beads were analyzed using a BD LSRFortessa cell analyzer.

AFM for measuring SynVAC-pMHC mechanical properties

Measurements were acquired on a JPK NanoWizard 4a BioScience instrument using a Bruker SAA-SPH-1UM probe with a nominal spring constant of approximately 0.25 N m^{-1}. The spring constant of each probe was determined by laser Doppler velocimetry calibration. Young's modulus was calculated by fitting force–indentation data to the Hertz/Sneddon model in JPK Data Processing. For relaxation measurements, the probe position was held fixed after the force reached 10 nN. Force decay was recorded as a function of time.

X-ray photoelectron spectroscopy (XPS) analysis for SynVAC-pMHC composition

Beads were mounted in an Axis Ultra DLD spectrometer (Kratos Analytical) and analysed under ultrahigh vacuum using monochromatic Al Kα radiation with a photon energy of 1486.6 eV. Survey spectra were acquired to characterize surface elemental composition. High-resolution measurements covered the C 1s and Ca 2p regions, including the Ca $2p_3/_2$ and Ca $2p_1/_2$ components.

SEM imaging of the interactions between SynVAC-pMHC and ESO-T cells

Donor PBMC samples were assayed for HLA-A*0201 expression via FACS. Human $CD8^+$ T cells were isolated from PBMCs using a human $CD8^+$ T Cell Isolation Kit (Miltenyi Biotec), and ESO-T were sorted using FACS. ESO-T cells were stimulated with FRB for 2 h and then fixed using 4% glutaraldehyde at 4-degree °C for 2 h. Subsequent post-fixation with 1% osmium tetroxide was applied for another 2 h. After fixation, the T cells were rinsed with HEPES-C buffer and then dehydrated through a graduated series of ethanol concentrations (75, 85, and 95%), with each step lasting 30 min. The samples were then dried using a Tousimis Autosamdri-810 critical point dryer. The specimens were subsequently mounted on specimen stubs and sputter-coated with a gold layer for SEM imaging.

In vitro antigen-specific T cell expansion

De-identified healthy-donor PBMCs were obtained from the UCLA/CFAR Virology Core Laboratory and screened for HLA-A*0201 expression by flow cytometry. Monocytes were isolated using CD14 MicroBeads (Miltenyi Biotec) and differentiated using the Mo-DC Generation Toolbox (Miltenyi Biotec). Mature moDCs were incubated with SLLMWITQV peptide at 10 μg ml^{-1} for 6 h at 37 °C. Peptide concentration was selected from a concentration-response experiment (Supplementary Fig. 17). Cultures were initiated with 1×10^6 PBMCs in medium containing 100 IU ml^{-1} recombinant IL-2 (BioLegend). Cells were stimulated with FRBs, MRBs, SRBs or peptide-loaded moDCs. Beads were added at a bead-to-PBMC ratio of 1:1. Fresh medium containing 100 IU ml^{-1} IL-2 was supplied to maintain cell density below 2×10^6 cells ml^{-1}. At day 7, cells were restimulated with the same conditions as day 0. Cells were counted on days 3, 7, and 14. Expansion was expressed relative to the number seeded at culture initiation. PBMCs from three independent donors were evaluated in each experiment.

Flow cytometry analysis of T cells

Cell phenotypes were assessed at the indicated collection times using staining procedures adapted from ref. 27. Samples were treated with Human TruStain FcX (BioLegend; 1:100) before antibody labelling in PBS for 30 min on ice. The BioLegend antibody panel comprised CD4 (OKT4; 1:400), CD8 (SK1; 1:300), CD3 (HIT3a; 1:500), CD45RO (UCHL1; 1:200) and CD19 (HIB19; 1:200). Additional antibodies recognized CD69 (FN50; 1:50), CD45RA (HI100; 1:200), CD62L (DREG-56; 1:50), CD95 (G043H7; 1:100) and CD25 (BC96; 1:500).

Intracellular phosphorylation measurements used a fixation/permeabilization kit (BD Biosciences). Samples were acquired on a BD LSRII instrument and analysed in FlowJo v10. The gating strategy is presented in Supplementary Fig. 18.

In vitro tumor killing assay

Cytotoxicity was assessed using a luciferase-based assay. Tumor cells expressing firefly luciferase and GFP were plated at 1×10^4 cells per well in black, clear-bottom 96-well plates (Corning). Effector cells were added in T cell culture medium at the effector-to-target ratios indicated in the figure legends. After 24 h, D-luciferin (Caliper Life Sciences) was added to a final concentration of 150 μg ml^{-1}. Luminescence was measured using an Infinite M1000 reader (Tecan) to estimate the remaining viable tumor cells.

Enzyme-linked immunosorbent cytokine assays (ELISA)

Secreted IL-2, TNF-α, and IFN-γ were measured in culture supernatants using sandwich ELISAs adapted from a standard protocol from BD Biosciences. Assays used matched capture and biotinylated detection antibodies from BD Biosciences, streptavidin–HRP from Invitrogen and recombinant cytokine standards from eBioscience. Absorbance was measured at 450 nm using an Infinite M1000 reader (Tecan).

T cell infiltration assay

A tumor micro-organoid was generated using microfluidic chips with approximately 20 cells per droplet, as described previously[56,57]. The organoids were cultured in complete media for 2 days and then cocultured with the expanded ESO-T cells labeled with Cytolight Rapid Red dye (Sartorius) according to the manufacturer's protocol. Briefly, the dye vial was reconstituted in 20 μL of DMSO, then diluted tenfold in PBS. ESO-T cells were incubated at 37 °C with 5 μL of the diluted dye (final 1:500) in PBS for 25 min. After one PBS wash, cells were counted and resuspended in complete medium before being plated with tumor organoids at effector-to-target (E:T) ratios of 5:1 or 10:1. Images were taken at different time points using a Zeiss Axio Observer Z1 inverted fluorescence microscope and analyzed with ImageJ.

Immunofluorescent visualization of immune synapse formation

The expanded ESO-T cells were frozen in CryoStor® CS5 (STEMCELL technology) for 7 days before being thawed for experiments. After stimulation for 15–60 min, cells were collected onto 12-mm coverslips (Citoglas) coated with poly-L-lysine (Sigma-Aldrich). Cells were fixed in methanol for 5 min at −20 °C and blocked with 5% donkey serum in HEPES–C buffer. CD3ε was labelled using an anti-CD3ε antibody (Abcam, ab52959; 1:400) for 1 h at room temperature. After three washes with HEPES–CT buffer, samples were incubated for 1 h with Alexa Fluor 488 goat anti-rabbit IgG and Alexa Fluor 647 goat anti-mouse IgG. Nuclei were labelled with DAPI (Thermo Fisher Scientific, D3571; 1:5000) for 5 min. Images were acquired using a Leica SP8-STED confocal microscope and quantified in ImageJ. CD3ε recruitment was calculated as the background-corrected proximal mean fluorescence intensity divided by the background-corrected distal mean fluorescence intensity.

Metabolites panel assay

2×10^6 ESO-T cells activated for 2 days were vacuum filtered onto nylon membranes (0.45 μm). Each filter was submerged, cell-side down, in 400 μl of precooled extraction solvent (40:40:20 acetonitrile/methanol/water) at −20 °C for 20 min. After washing, metabolite extracts were collected, centrifuged at 17,000 × *g*, dried under nitrogen gas, and reconstituted in HPLC-grade water (10–15 μl per 10^6 cells).

Cell extracts were analyzed by ultra-high-performance liquid chromatography (UHPLC) coupled to a Q Exactive Plus mass spectrometer (UHPLC-MS) with electrofspray ionization and randomized sample injection. LC separation used an XBridge BEH Amide XP column and a gradient of solvent A (aqueous, pH 9.4) and solvent B (acetonitrile). Two flow paths were operated in tandem, staggered by 20 min. The 5 μl injection was run at 150 μl min^{-1}. The mass spectrometer operated in negative- and positive-ion modes with a resolution of 140,000 and a scan range of m/z 60–2000. Data was collected with Xcalibur and analyzed using MAVEN, with identification and integration based on retention times from authenticated standards.

FLIM imaging

Fluorescence lifetime imaging was performed on a Leica STELLARIS 8 Fast Lifetime Contrast (FALCON) inverted microscope (previously Leica SP8 FALCON) equipped with a live-cell workstation (37 °C, 5% CO_2; Tokai Hit, Japan). Instrument response function correction is built into the system design. To validate performance, Coumarin 6 dye was routinely measured before imaging, serving as a standard to confirm accurate lifetime detection at ~2.5 ns on the phasor semicircle. Intracellular NAD(P)H and FAD autofluorescence were excited in two-photon mode at 740 nm. Before imaging, cells were balanced in RPMI 1640 supplemented with 10% FBS for 3 h to avoid autofluorescence from HEPES. Emission was collected using 460/80 nm (NAD(P)H) and 540/50 nm (FAD) bandpass filters. The laser source (1.8 W) was carefully attenuated to 0.5 mW at the objective lens exit aperture, as measured with a Thorlabs photopower meter, to minimize

photobleaching and cell damage. FLIM images were acquired at a pixel size of 284 nm and dwell time of 7.69 μs, with 8× line averaging to improve signal-to-noise ratio.

Confocal and TEM imaging of mitochondria

For confocal imaging, 1×10^6 ESO-T cells activated for 2 days were stained with 0.6 ml of phenol red-free RPMI 1640 (ThermoFisher) containing 50 nM MitoTracker Green (ThermoFisher), 0.5 mg/mL Hoechst, and 7.5 μM Tetramethylrhodamine, Methyl Ester, Perchlorate (TMRM) (ThermoFisher) for 1 h in a cell incubator. Cells were then washed once with PBS and immediately sent to the UCLA Metabolism Core for imaging.

For TEM imaging, 1×10^6 cells activated with SynVAC-pMHC were centrifuged and washed once with PBS. 1 ml PBS containing 2.5% glutaraldehyde and 2% paraformaldehyde was then added to fix cells for 30 min. Samples were then washed with PBS twice and sent to the UCLA Metabolism Core for subsequent slicing, staining, and imaging.

XFe96 seahorse assay

The ESO-T cells are sorted from the expanded T cell population by FACS, and frozen at −80 °C one week before thawing. ESO-T cells are co-cultured with FRB, MRB, or SRB for 1 or 2 days before sending them to the UCLA Metabolism Core. The cells were subsequently spun down into a poly-lysine-treated 96-well plate at $300 \times g$ for 5 min, with 2.5×10^5 cells in each well. The culture plate was then introduced into the tray of the Seahorse XFe96 analyzer, and the acquisition program was run. This program includes an equilibration step, followed by measurements at basal, post-oligomycin injection, and post-FCCP injection. Each of these three steps comprises three loops: three minutes of mixing, two minutes of waiting, and three minutes of measuring. Data were analyzed using Wave 2.6.1 Software (Agilent Technologies).

RNA sequencing

For single-cell RNA sequencing, T cells were collected on day 14 after stimulation with SynVAC-pMHC or moDCs. Samples were processed by the UCLA Technology Center for Genomics and Bioinformatics Core. Sequencing was performed using the 10× Genomics Chromium™ Controller Single Cell Sequencing System, following the manufacturer's instructions and the TCGB Core's standard protocol. Library preparation was carried out with the Illumina TruSeq RNA Sample Prep Kit (Cat#FC-122-1001), and sequencing was performed on an Illumina NovaSeq system with 150 bp paired-end reads (20,000 reads per cell). Read alignment to the human reference genome (GRCh38) was performed using CellRanger.

For bulk RNA sequencing, cells activated by SynVAC-pMHC were harvested at 6 or 24 h post-activation and sent to the UCLA TCGB core for bulk RNA sequencing. Library was constructed with a stranded, poly(A)-selected RNA library preparation following the manufacturer's instruction. Sequencing was performed on Illumina NovaSeq X Plus system with 10B reads. Read alignment to the human reference genome (GRCh38) was performed using Spliced Transcripts Alignment to a Reference (STAR) (v2.7.11b).

The processed cell matrix and associated metadata have been deposited in the Gene Expression Omnibus database (GSE324103).

In vivo anti-tumor efficacy study of ESO-T cells in human OVCAR3 and melanoma xenograft NSG mouse models

NSG mice (NOD.Cg-Prkdc^scid Il2rg^tm1Wjl/SzJ) were maintained under specific pathogen-free conditions. Housing temperature was 68–79 °F, relative humidity was 30–70%, and rooms were maintained under negative pressure. A 12-h light/dark cycle was used, with lights on at 06:00. Experiments used male and female mice aged 6–10 weeks. Sex was not included as an experimental variable because no significant sex-dependent differences were observed in the NSG mouse models used in this study. All animal procedures were approved by the UCLA Institutional Animal Care and Use Committee. Mice were bred and maintained under specific pathogen-free conditions, and all experiments were conducted in accordance with the animal care and use regulations of the UCLA Division of Laboratory Animal Medicine. Maximal tumor burden for OVCAR3-FG mouse model is determined by empirical value of the lab (maximal BLI value is 3×10^{10} photons/second), where the mouse will be euthanized after reaching the clinical humane endpoint. Maximal tumor size for A375-FG is 1000 mm^3. Maximal tumor size/burden was not exceeded during the study.

The experimental design is illustrated in Fig. 6a and h. Briefly, on day 0, NSG mice were intraperitoneally (i.p.) inoculated with OVCAR3-FG or subcutaneously (s.c.) inoculated with A375-FG cells (1×10^6 cells per mouse). On day 7, the mice received an intravenous (i.v.) injection of either vehicle control (100 μl PBS per mouse) or ESO-T cells (3×10^6 ESO-T cells in 100 μl PBS per mouse). Tumor burden was monitored over time using bioluminescence imaging (BLI). Mice were euthanized on day 60 for the OVCAR3-FG model or day 32 for the A375-FG model, and tissues were collected for analysis.

In vivo bioluminescence imaging (BLI)

Bioluminescence was acquired using a Spectral AMI HTX imaging system (Spectral Instruments Imaging). Whole-body imaging was performed 5 min after intraperitoneal administration of D-luciferin at 1 mg per mouse. Tissue-specific imaging was performed 15 min after administration of 3 mg per mouse. Images were quantified using AURA software.

Statistical analysis

Data are presented as mean ± SEM. Statistical significance between two groups was determined using a two-tailed Student's *t*-test in GraphPad Prism 10. For comparisons involving more than two groups, one-way analysis of variance (ANOVA) was performed, followed by Tukey's multiple comparison test. Two-way ANOVA was used to analyze differences among multiple groups with two independent variables. Statistical significance was defined as follows: not significant ($P > 0.05$); *$P < 0.05$; **$P < 0.01$; ***$P < 0.001$; ****$P < 0.0001$. Unless otherwise stated, "*n*" represents independent experimental replicates performed using cells from the same donor.

Reporting summary

Further information on research design is available in the Nature Portfolio Reporting Summary linked to this article.

Data availability

The sequencing data generated during this study is available from the Gene Expression Omnibus database (GSE324103). The metabolites data is available from the MetaboLights database (MTBLS15444). The remaining data associated with this study are present in the article, its Supplementary Information, or Source Data file. Source data are provided with this paper.

References

1. Chandran, S. S. & Klebanoff, C. A. T cell receptor-based cancer immunotherapy: emerging efficacy and pathways of resistance. *Immunol. Rev.* **290**, 127–147 https://doi.org/10.1111/imr.12772 (2019).
2. Liu, Z. et al. Engineering biomaterials for next-generation cancer immunotherapy: from cell manufacturing to in vivo modulation. *Cell Biomater*. https://doi.org/10.1016/j.celbio.2026.100380 (2026).
3. Zhu, E., Liu, Z. & Li, Y.-R. Feeder-free advances in T cell development and therapy. *Cell Biomater.* **2** https://doi.org/10.1016/j.celbio.2025.100244 (2026).

4. Stone, J. D. & Kranz, D. M. Role of T cell receptor affinity in the efficacy and specificity of adoptive T cell therapies. *Front. Immunol.* **4**, 244 https://doi.org/10.3389/fimmu.2013.00244 (2013).
5. Kim, G. B. et al. Quantitative immunopeptidomics reveals a tumor stroma–specific target for T cell therapy. *Sci. Transl. Med.* **14**, eabo6135 https://doi.org/10.1126/scitranslmed.abo6135 (2022).
6. Mazzoccoli, L. & Liu, B. Dendritic cells in shaping anti-tumor T cell response. *Cancers* **16**, 2211 https://doi.org/10.3390/cancers16122211 (2024).
7. Sabado, R. L., Balan, S. & Bhardwaj, N. Dendritic cell-based immunotherapy. *Cell Res.* **27**, 74–95 https://doi.org/10.1038/cr.2016.157 (2017).
8. Li, Y. & Kurlander, R. J. Comparison of anti-CD3 and anti-CD28-coated beads with soluble anti-CD3 for expanding human T cells: differing impact on CD8 T cell phenotype and responsiveness to restimulation. *J. Transl. Med.* **8**, 104 https://doi.org/10.1186/1479-5876-8-104 (2010).
9. Mock, U. et al. Automated manufacturing of chimeric antigen receptor T cells for adoptive immunotherapy using CliniMACS prodigy. *Cytotherapy* **18**, 1002–1011 https://doi.org/10.1016/j.jcyt.2016.05.009 (2016).
10. Oelke, M. et al. Ex vivo induction and expansion of antigen-specific cytotoxic T cells by HLA-Ig–coated artificial antigen-presenting cells. *Nat. Med.* **9**, 619–625 https://doi.org/10.1038/nm869 (2003).
11. Wang, H. & Mooney, D. J. Biomaterial-assisted targeted modulation of immune cells in cancer treatment. *Nat. Mater.* **17**, 761–772 https://doi.org/10.1038/s41563-018-0147-9 (2018).
12. Huse, M. Mechanoregulation of lymphocyte cytotoxicity. *Nat. Rev. Immunol.* **25**, 680–695 https://doi.org/10.1038/s41577-025-01173-2 (2025).
13. Zhang, X. et al. Unraveling the mechanobiology of immune cells. *Curr. Opin. Biotechnol.* **66**, 236–245 https://doi.org/10.1016/j.copbio.2020.09.004 (2020).
14. Adebowale, K. et al. Enhanced substrate stress relaxation promotes filopodia-mediated cell migration. *Nat. Mater.* **20**, 1290–1299 https://doi.org/10.1038/s41563-021-00981-w (2021).
15. Liu, Z. et al. Mechanomedicine. *Nat. Rev. Bioeng.* **4**, 216–235 https://doi.org/10.1038/s44222-025-00391-6 (2026).
16. Liu, Y. et al. DNA-based nanoparticle tension sensors reveal that T-cell receptors transmit defined pN forces to their antigens for enhanced fidelity. *Proc. Natl. Acad. Sci. USA* **113**, 5610–5615 https://doi.org/10.1073/pnas.1600163113 (2016).
17. Basu, R. et al. Cytotoxic T cells use mechanical force to potentiate target cell killing. *Cell* **165**, 100–110 https://doi.org/10.1016/j.cell.2016.01.021 (2016).
18. Tello-Lafoz, M. et al. Cytotoxic lymphocytes target characteristic biophysical vulnerabilities in cancer. *Immunity* **54**, 1037–1054.e1037 https://doi.org/10.1016/j.immuni.2021.02.020 (2021).
19. Liu, Y. et al. Cell softness prevents cytolytic T-cell killing of tumor-repopulating cells. *Cancer Res* **81**, 476–488 https://doi.org/10.1158/0008-5472.Can-20-2569 (2021).
20. Liu, B., Chen, W., Evavold, B. rianD. & Zhu, C. Accumulation of dynamic catch bonds between TCR and agonist peptide-MHC triggers T cell signaling. *Cell* **157**, 357–368 https://doi.org/10.1016/j.cell.2014.02.053 (2014).
21. Zhu, C., Chen, W., Lou, J., Rittase, W. & Li, K. Mechanosensing through immunoreceptors. *Nat. Immunol.* **20**, 1269–1278 https://doi.org/10.1038/s41590-019-0491-1 (2019).
22. Jeffreys, N., Brockman, J. M., Zhai, Y., Ingber, D. E. & Mooney, D. J. Mechanical forces amplify TCR mechanotransduction in T cell activation and function. *Appl Phys. Rev.* **11**, 011304 https://doi.org/10.1063/5.0166848 (2024).
23. Feng, Y., Reinherz, E. L. & Lang, M. J. αβ T cell receptor mechanosensing forces out serial engagement. *Trends Immunol.* **39**, 596–609 https://doi.org/10.1016/j.it.2018.05.005 (2018).
24. Lou, J. et al. Surface-functionalized microgels as artificial antigen-presenting cells to regulate expansion of T cells. *Adv. Mater.* **36**, 2309860 https://doi.org/10.1002/adma.202309860 (2024).
25. Hasani-Sadrabadi, M. M. et al. Harnessing biomaterials to amplify immunity in aged mice through T memory stem cells. *ACS Nano* **18**, 6908–6926 https://doi.org/10.1021/acsnano.3c08559 (2024).
26. Yuan, D. J., Shi, L. & Kam, L. C. Biphasic response of T cell activation to substrate stiffness. *Biomaterials* **273**, 120797 https://doi.org/10.1016/j.biomaterials.2021.120797 (2021).
27. Liu, Z. et al. Viscoelastic synthetic antigen-presenting cells for augmenting the potency of cancer therapies. *Nat. Biomed. Eng.* **8**, 1615–1633 https://doi.org/10.1038/s41551-024-01272-w (2024).
28. Adu-Berchie, K. et al. Generation of functionally distinct T-cell populations by altering the viscoelasticity of their extracellular matrix. *Nat. Biomed. Eng.* **7**, 1374–1391 https://doi.org/10.1038/s41551-023-01052-y (2023).
29. Cribioli, E. et al. Enforcing GLUT3 expression in CD8(+) T cells improves fitness and tumor control by promoting glucose uptake and energy storage. *Front. Immunol.* **13**, 976628 https://doi.org/10.3389/fimmu.2022.976628 (2022).
30. Beumer-Chuwonpad, A. et al. Memory CD8(+) T cells upregulate glycolysis and effector functions under limiting oxygen conditions. *Eur. J. Immunol.* **53**, e2249918 https://doi.org/10.1002/eji.202249918 (2023).
31. Xia, L., Lee, C. & Li, J. J. Statistical method scDEED for detecting dubious 2D single-cell embeddings and optimizing t-SNE and UMAP hyperparameters. *Nat. Commun.* **15**, 1753 https://doi.org/10.1038/s41467-024-45891-y (2024).
32. Jalili, S. et al. Leveraging tissue-resident memory T cells for non-invasive immune monitoring via microneedle skin patches. *Nat. Biomed. Eng.* https://doi.org/10.1038/s41551-026-01617-7 (2026).
33. Subramanian, A. et al. Gene set enrichment analysis: a knowledge-based approach for interpreting genome-wide expression profiles. *Proc. Natl. Acad. Sci. USA* **102**, 15545–15550 https://doi.org/10.1073/pnas.0506580102 (2005).
34. Ashburner, M. et al. Gene Ontology: tool for the unification of biology. *Nat. Genet.* **25**, 25–29 https://doi.org/10.1038/75556 (2000).
35. Aleksander, S. A. et al. The Gene Ontology knowledgebase in 2023. *Genetics* **224** https://doi.org/10.1093/genetics/iyad031 (2023).
36. Dustin, M. L. The immunological synapse. *Cancer Immunol. Res.* **2**, 1023–1033 https://doi.org/10.1158/2326-6066.Cir-14-0161 (2014).
37. Grakoui, A. et al. The immunological synapse: a molecular machine controlling T cell activation. *Science* **285**, 221–227 https://doi.org/10.1126/science.285.5425.221 (1999).
38. Love, M. I., Huber, W. & Anders, S. Moderated estimation of fold change and dispersion for RNA-seq data with DESeq2. *Genome Biol.* **15**, 550 https://doi.org/10.1186/s13059-014-0550-8 (2014).
39. Ge, X. et al. Clipper: p-value-free FDR control on high-throughput data from two conditions. *Genome Biol.* **22**, 288 https://doi.org/10.1186/s13059-021-02506-9 (2021).
40. Schaefer, C. F. et al. PID: the pathway interaction database. *Nucleic Acids Res.* **37**, D674–D679 https://doi.org/10.1093/nar/gkn653 (2009).
41. Garçon, F. et al. CD28 provides T-cell costimulation and enhances PI3K activity at the immune synapse independently of its capacity to interact with the p85/p110 heterodimer. *Blood* **111**, 1464–1471 https://doi.org/10.1182/blood-2007-08-108050 (2008).
42. Colombetti, S., Basso, V., Mueller, D. L. & Mondino, A. Prolonged TCR/CD28 engagement drives IL-2-independent T cell clonal expansion through signaling mediated by the mammalian target of

rapamycin. *J. Immunol.* **176**, 2730–2738 https://doi.org/10.4049/jimmunol.176.5.2730 (2006).
43. Chen, Y. et al. Regulation of CD8+ T memory and exhaustion by the mTOR signals. *Cell. Mol. Immunol.* **20**, 1023–1039 https://doi.org/10.1038/s41423-023-01064-3 (2023).
44. Chi, H. Regulation and function of mTOR signalling in T cell fate decisions. *Nat. Rev. Immunol.* **12**, 325–338 https://doi.org/10.1038/nri3198 (2012).
45. Pollizzi, K. N., Waickman, A. T., Patel, C. H., Sun, I. H. & Powell, J. D. Cellular size as a means of tracking mTOR activity and cell fate of CD4+ T cells upon antigen recognition. *PLoS One* **10**, e0121710 https://doi.org/10.1371/journal.pone.0121710 (2015).
46. Pearce, E. L. Metabolism in T cell activation and differentiation. *Curr. Opin. Immunol.* **22**, 314–320 https://doi.org/10.1016/j.coi.2010.01.018 (2010).
47. Pham, D. L. et al. Label-free metabolic imaging monitors the fitness of chimeric antigen receptor T cells. *Nat. Biomed. Eng.* **10**, 785–802 https://doi.org/10.1038/s41551-025-01504-7 (2025).
48. Zhou, H. Label-free metabolic optical biomarkers track stem cell fate transition in real time. *Sci. Adv.* **10**, eadi6770 https://doi.org/10.1126/sciadv.adi6770.
49. Buck, M. D. et al. Mitochondrial dynamics controls T cell fate through metabolic programming. *Cell* **166**, 63–76 https://doi.org/10.1016/j.cell.2016.05.035 (2016).
50. Blumenthal, D., Chandra, V., Avery, L. & Burkhardt, J. K. Mouse T cell priming is enhanced by maturation-dependent stiffening of the dendritic cell cortex. *eLife* **9**, e55995 https://doi.org/10.7554/eLife.55995 (2020).
51. Peng, M. et al. Aerobic glycolysis promotes T helper 1 cell differentiation through an epigenetic mechanism. *Science* **354**, 481–484 https://doi.org/10.1126/science.aaf6284 (2016).
52. Tyrakis, P. A. et al. S-2-hydroxyglutarate regulates CD8+ T-lymphocyte fate. *Nature* **540**, 236–241 https://doi.org/10.1038/nature20165 (2016).
53. Roy, D. G. et al. Methionine metabolism shapes T helper cell responses through regulation of epigenetic reprogramming. *Cell Metab.* **31**, 250–266.e259 https://doi.org/10.1016/j.cmet.2020.01.006 (2020).
54. Liu, Z. et al. Manufacturing synthetic viscoelastic antigen-presenting cells for immunotherapy. *Nat. Protoc.* **21**, 2960–2994 https://doi.org/10.1038/s41596-025-01265-2 (2025).
55. Li, Y.-R. et al. Generation of allogeneic CAR-NKT cells from hematopoietic stem and progenitor cells using a clinically guided culture method. *Nat. Biotechnol.* **43**, 329–344 https://doi.org/10.1038/s41587-024-02226-y (2025).
56. Ding, S. et al. Patient-derived micro-organospheres enable clinical precision oncology. *Cell Stem Cell* **29**, 905–917.e906 https://doi.org/10.1016/j.stem.2022.04.006 (2022).
57. Wang, Z. et al. Rapid tissue prototyping with micro-organospheres. *Stem Cell Rep.* **17**, 1959–1975 https://doi.org/10.1016/j.stemcr.2022.07.016 (2022).

Acknowledgements

We thank the UCLA Division of Laboratory Animal Medicine (DLAM) for providing animal support, the UCLA Metabolism core for providing cell metabolism characterization, the UCLA BSCRC Flow Cytometry Core Facility for providing cell sorting support, the UCLA TCGB facility for providing scRNAseq services, the UCLA Center for AIDS Research (CFAR) Virology Core for providing human PBMCs, and the Advanced Light Microscopy/Spectroscopy Laboratory, the Electron Imaging Center for Nanosystems, and the Nano and Pico Characterization Laboratory at the California NanoSystems Institute (CNSI) for supporting the image acquisition. We also thank the NIH Tetramer Facility for providing the peptide-MHC tetramers.

Author contributions

Y.Y., Z.L., Y.-R.L., L.Y., and S.L. designed the experiments. Y.Y., Y.-R.L., Z.L., H.Z., Y.Z., X.S., D.L., E.-Z.M., H.N., B.Z., S.W., J.L., Y.C., B.R., E.Z., and J.S. performed the experiments. Y.Y., Y.R.L., Z.L., Y.C., E.Z., and J.S. analyzed the data; Y.Y., Y.-R.L., and Z.L. interpreted the results. Y.Y., Z.L., and Y.-R.L. wrote the original draft. S.L., L.Y., K.S., J.-O.P., J.-J.L., X.S., Z.W., H.Z., Y.Z., X.S., D.L., E.-Z.M., H.N., B.Z., S.W., J.L., Y.C., E.Z., and J.S. reviewed and edited the final draft.

Funding

This work was supported in part by a UCLA Jonsson Comprehensive Cancer Center (JCCC) Seed Grant (to S.L. and L.Y.), a UCLA Broad Stem Cell Research Center (BSCRC) Innovation Award (to S.L.), a grant from the National Institutes of Health (NIH) (GM143485 to S.L.), a Discovery Stage Award from the California Institute for Regenerative Medicine (CIRM) (DISC2-14169 to S.L.), an Ablon Scholars Award (to L.Y.), a grant from the National Institutes of Health (NIH) (R01CA220012 to K.S.), a USC Ming Hsieh Institute Research Award (to K.S.), a Mann Engineering in Medicine Pilot Grant (to K.S.), a grant from the National Institutes of Health (NIH) (R35GM143127 to J.-O.P.), and a NIH instrumentation grant (1S10OD016387-01 to J.-O.P.). Y.-R.L. is a postdoctoral fellow supported by a UCLA Microbiology, Immunology, and Molecular Genetics M. John Pickett Post-Doctoral Fellow Award and a CIRM-BSCRC Postdoctoral Fellowship. H.Z. is a postdoctoral fellow supported by a CIRM Post-doctoral Fellowship.

Competing interests

L.Y. is a scientific advisor to AlzChem and Amberstone Biosciences, and a co-founder, stockholder, and advisory board member of Appia Bio. None of the declared companies contributed to or directed any of the research reported in this article. The remaining authors declare no competing interests.

Additional information

Supplementary information The online version contains supplementary material available at https://doi.org/10.1038/s41467-026-78131-6.

Correspondence and requests for materials should be addressed to Lili Yang or Song Li.

Peer review information *Nature Communications* thanks Paolo P. Provenzano and the other, anonymous, reviewer(s) for their contribution to the peer review of this work. A peer review file is available.

Reprints and permissions information is available at http://www.nature.com/reprints

Publisher's note Springer Nature remains neutral with regard to jurisdictional claims in published maps and institutional affiliations.

Open Access This article is licensed under a Creative Commons Attribution 4.0 International License, which permits use, sharing, adaptation, distribution and reproduction in any medium or format, as long as you give appropriate credit to the original author(s) and the source, provide a link to the Creative Commons licence, and indicate if changes were made. The images or other third party material in this article are included in the article's Creative Commons licence, unless indicated otherwise in a credit line to the material. If material is not included in the article's Creative Commons licence and your intended use is not permitted by statutory regulation or exceeds the permitted use, you will need to obtain permission directly from the copyright holder. To view a copy of this licence, visit http://creativecommons.org/licenses/by/4.0/.

© The Author(s) 2026

This Article in Press is shared early to give you faster access to new research. It is citable and carries a permanent DOI. The final edited version will replace it automatically.

[1]Department of Bioengineering, University of California, Los Angeles, Los Angeles, CA, USA. [2]Department of Microbiology, Immunology & Molecular Genetics, University of California, Los Angeles, Los Angeles, CA, USA. [3]Alfred E. Mann Department of Biomedical Engineering, University of Southern California, Los Angeles, CA, USA. [4]Eli & Edythe Broad CIRM Center for Regenerative Medicine& Stem Cell Research, University of Southern California, Los Angeles, CA, USA. [5]Department of Chemical and Biomolecular Engineering, University of California, Los Angeles, Los Angeles, CA, USA. [6]Department of Computational Medicine, University of California, Los Angeles, Los Angeles, CA, USA. [7]Terasaki Institute for Biomedical Innovation, Woodland Hills, CA, USA. [8]Department of Materials Science and Engineering, University of California, Los Angeles, Los Angeles, CA, USA. [9]Department of Chemistry and Biochemistry, University of California, Los Angeles, Los Angeles, CA, USA. [10]Norris Comprehensive Cancer Center, University of Southern California, Los Angeles, CA, USA. [11]Biostatistics Program, Public Health Sciences Division, Fred Hutchinson Cancer Center, Seattle, WA, USA. [12]Molecular Biology Institute, University of California, Los Angeles, Los Angeles, CA, USA. [13]Eli and Edythe Broad Center of Regenerative Medicine and Stem Cell Research, University of California, Los Angeles, Los Angeles, CA, USA. [14]Jonsson Comprehensive Cancer Center, David Geffen School of Medicine, University of California, Los Angeles, Los Angeles, CA, USA. [15]These authors contributed equally: Youcheng Yang, Yan-Ruide Li, Zeyang Liu. ✉e-mail: liliyang@ucla.edu; songli@ucla.edu